Astronomy & Astrophysics manuscript no. califa_grads_rv
May 19, 2016

The dependence of oxygen and nitrogen abundances on stellar mass from the CALIFA survey ⋆

E. Pérez-Montero ⋆⋆[1], R. García-Benito[1], J.M. Vílchez[1], S. F. Sánchez[1,2], C. Kehrig[1], B. Husemann[3], S. Duarte Puertas[1], J. Iglesias-Páramo[1], L. Galbany[4,5], M. Mollá[6], C. J. Walcher[3], Y. Ascasíbar[7], R. M. González Delgado[1], R. A. Marino[8,9], J. Masegosa[1], E. Pérez[1], F. F. Rosales-Ortega[10], P. Sánchez-Blázquez[7,11], J. Bland-Hawthorn[12], D. Bomans[13], Á. R. López-Sánchez[14,15], B. Ziegler[16], and The CALIFA collaboration

[1] Instituto de Astrofísica de Andalucía - CSIC. Apdo. de correos 3004, E-18080, Granada, Spain
[2] Instituto de Astronomía,Universidad Nacional Autonóma de Mexico, A.P. 70-264, 04510, México,D.F.
[3] Leibniz-Institut für Astrophysik Potsdam (AIP), An der Sternwarte 16, D-14482 Potsdam, Germany.
[4] Millennium Institute of Astrophysics. Chile
[5] Departamento de Astronomía, Universidad de Chile, Camino El Observatorio 1515, Las Condes, Santiago, Chile
[6] Departamento de Investigación Básica, CIEMAT, Avda. Complutense 40 E-28040 Madrid, Spain.
[7] Departamento de Física Teórica, Universidad Autónoma de Madrid, 28049 Madrid, Spain.
[8] Department of Physics, Institute for Astronomy, ETH Zürich, CH-8093, Zürich, Switzerland
[9] Departamento de Astrofísica y CC. de la Atmósfera, Facultad de CC. Físicas, Universidad Complutense de Madrid, Avda. Complutense s/n, 28040 Madrid, Spain.
[10] Instituto Nacional de Astrofísica, Óptica y Electrónica, Luis E. Erro 1, 72840 Tonantzintla, Puebla, Mexico
[11] Instituto de Astrofísica, Facultad de Física, Pontificia Universidad Católica de Chile, 4860 Av. Vicuña Mackenna, Santiago, Chile.
[12] Sydney Institute for Astronomy, School of Physics A28, University of Sydney, NSW 2006, Australia.
[13] Astronomical Institute of the Ruhr-University Bochum Universitaetsstr. 150, 44801 Bochum, Germany.
[14] Australian Astronomical Observatory, PO Box 915, North Ryde, NSW 1670, Australia
[15] Department of Physics and Astronomy, Macquarie University, NSW 2109, Australia
[16] University of Vienna, Türkenschanzstrasse 17, 1180 Vienna, Austria.

Received: —, Accepted: —

ABSTRACT

Context. The study of the integrated properties of star-forming galaxies is central to understand their formation and evolution. Some of these properties are extensive and therefore their analysis require from totally-covering and spatially-resolved observations. Among them, metallicity can be defined in spiral discs by means of integral field spectroscopy (IFS) of individual H ii regions. The simultaneous analysis of the abundances of primary elements, as oxygen, and secondary, as nitrogen, also gives clues on the star formation history and the processes that shape the build-up of spiral discs.

Aims. Our main aim is to analyse simultaneously O/H and N/O abundance ratios in H ii regions in different radial positions of the discs in a large sample of spiral galaxies to obtain the slopes and the characteristic abundance ratios that can be related with their integrated properties.

Methods. We analysed the optical spectra of individual selected H ii regions extracted from a sample of 350 spiral galaxies of the CALIFA survey. We calculated total O/H abundances and, for the first time, N/O ratios using the semi-empirical routine Hii-Chi-mistry, **which, according to Pérez-Montero (2014),** is consistent with the direct method and reduces the uncertainty in the O/H derivation using [N ii] lines owing to the dispersion in the O/H-N/O relation. Then we performed linear fittings to the abundances as a function of the de-projected galactocentric distances.

Results. The analysis of the radial distribution both for O/H and N/O in the non-interacting galaxies reveals that both average slopes are negative, but with a non-negligible fraction of objects having a flat or even a positive gradient (at least 10% for O/H and 4% for N/O). The slopes normalised to the effective radius look to have a slight dependence on the total stellar mass and the morphological type, as late low-mass objects tend to have flatter slopes, but no clear relation is found to explain the presence of inverted gradients in this sample. No dependence between the average slopes and the presence of a bar. The relation between the resulting O/H and N/O linear fittings at the effective radius is much tighter (correlation coefficient ρ_s = 0.80) than between O/H and N/O slopes (ρ_s = 0.39) or for O/H and N/O in the individual H ii regions (ρ_s = 0.37). These O/H and N/O values at the effective radius also correlate very tightly (less than 0.03 dex of dispersion) with total luminosity and stellar mass. The relation with other integrated properties ,such as star-formation rate, colour or morphology, can be understood only on the light of the found relation with mass.

Key words. H ii regions / galaxies: ISM / ISM: abundances / galaxies: abundances / galaxies: evolution / galaxies: star formation

Send offprint requests to: E. Pérez-Montero e-mail: `epm@iaa.es`

⋆ Based on observations collected at the Centro Astronómico Hispano Alemán (CAHA) at Calar Alto, operated jointly by the Max-Planck Institut für Astronomie and the Instituto de Astrofísica de Andalucía (CSIC).

⋆⋆ epm@iaa.es

1. Introduction

The study of galaxy formation and evolution through different cosmological epochs is nowadays a hot topic of research. The amount of available data coming from large ground and space telescopes at increasingly higher redshift (z) and better spatial resolution is growing substantially thanks to many deep sky surveys as zCOSMOS (Lilly et al. 2007), MASSIV (Contini et al. 2012), MANGA (Bundy et al. 2015) or SAMI (Bryant et al. 2015). Among the different integrated properties of galaxies to investigate, one of special interest to understand their evolutionary status and the pathway followed towards their current state is their metal content. Metallicity (Z) is a crucial parameter since its value is the fruit of the conversion of unprocessed gas onto stars, which transform light into heavier elements and spew them out into the interstellar medium (ISM) or even into the intergalactic medium (IGM) to take possibly part in a new loop of star formation and chemical enrichment. Z then traces the age, star formation history and efficiency of galaxies, and it is therefore linked to their other integrated properties (e.g.Roberts & Haynes 1994).

A thorough dissection of the observed integrated properties in the galaxies of the Local Universe gives us the opportunity to look deeper into the fundamental relations observed in a Universe at larger z under a new light.

In this way, the integrated values of extensive properties and the spatial distribution of intensive properties, that are not always homogeneous, can be investigated in local galaxies. In the case of Z, it is known to correlate with the total luminosity (e.g. Lequeux et al. 1979; Skillman 1989; Lamareille et al. 2004) and the total stellar mass of galaxies (e.g. Tremonti et al. 2004). These correlations were found to exist even in spiral galaxies, where spectroscopy of individual H ii regions helps to trace a negative gradient of Z (e.g. Garnett & Shields 1987; Vila-Costas & Edmunds 1992; Zaritsky et al. 1994; Marino et al. 2012). Despite the slopes of these gradients are found to be steeper for fainter galaxies (Garnett et al. 1997), a common mass-independent slope can be obtained when the slope is divided by the effective or the isophotal radius (e.g. Diaz 1989; Sánchez et al. 2014) and one can recover for each galaxy a characteristic Z value that also correlates with their integrated properties (e.g. Pilyugin et al. 2004; Moustakas & Kennicutt 2006). This normalisation has been also used by several authors to propose a common slope for all non-interacting disc galaxies (e.g. Bresolin et al. 2009; Rosales-Ortega et al. 2011; Bresolin et al. 2012; Sánchez et al. 2014; Ho et al. 2015; Marino et al. 2016). This could be consistent with a common inside-out scenario of growth of the disc owing to the fall of gas from the halo in all galaxies (e.g. Pichon et al. 2011).

However there are some indications that the steepness of the gradient of Z in galaxy discs, and hence the derivation of a characteristic value, can be influenced by other factors. Among them, they have been proposed the presence of a bar or the morphological type (e.g. Vila-Costas & Edmunds 1992; Zaritsky et al. 1994), although also see Sánchez et al. (2014). There are also evidences for the presence of flat or even inverted gradients in interacting galaxies (e.g. Rich et al. 2012; López-Sánchez et al. 2015) or in some low-mass and/or gas-rich galaxies (e.g. Werk et al. 2010, 2011; Moran et al. 2012). On the other hand, Carton et al. (2015) find steeper gradients in gas-rich galaxies. According to the study of the radial distribution of metals at higher z the fraction of galaxies with an inverted or a flat gradient could be higher owing to a higher rate of interactions and mergers in a denser Universe (Cresci et al. 2010; Queyrel et al. 2012; Troncoso et al. 2014).

When Z is obtained from the optical spectra of H ii regions it is usually expressed in terms of the abundance of a primary element as oxygen (12+log(O/H), hereafter O/H). Nevertheless, exploring at same time the spatial variation of the chemical abundance ratio of a primary element o a secondary element, as nitrogen (log(N/O), hereafter N/O), can shed some light on the origin of the flattening or the inversion of chemical gradients in discs and the global relations with the galactic integrated properties. Edmunds (1990) shows that this kind of ratio could be relatively unaffected by hydrodynamical effects, such as infalls of metal-poor gas or outflows of enriched material. This makes the relation between N/O and the integrated stellar mass (hereafter MNOR, Pérez-Montero & Contini 2009) to correlate even in those galaxies whose Z is dissevered from its star formation history (Köppen & Hensler 2005), such as in some extreme emission line galaxies (e.g. Amorín et al. 2010; Pérez-Montero et al. 2011). In this way the MNOR, contrary to the mass-metallicity relation (MZR), does not have any dependence on the integrated star formation rate (SFR) (Pérez-Montero et al. 2013).

Over and above, the study of the spatial variation of N/O can help to derive more accurate abundance gradients in spatially-resolved galaxies. Since N spreads over a much wider range of variation than O (e.g. Thuan et al. 2010) its study can be achieved at a better precision from the analysis of the emission lines from H ii regions. **In addition, possible deviations from the typical O/H-N/O relation (i.e. growing N/O for growing O/H in the production regime of secondary N)** can also be useful to explore variations in the star formation efficiency (Mollá et al. 2006), the stellar yields, or initial mass function (IMF) changes across discs (e.g. Mattsson 2009), as most of O is produced by short-living massive stars and most of N is ejected to the ISM by long-living low and intermediate-mass stars in the metal-rich discs of galaxies.

Inasmuch as we aim at investigating the behavior of the abundance gradients in local galaxies, we need a sufficiently large sample of objects covered in 2 dimensions with integral field spectroscopy (IFS) in the optical range, as it is the case of CALIFA (Calar Alto Legacy Integral Field Area survey, Sánchez et al. 2012a). The sample of galaxies studied in the CALIFA survey is well characterised and all integrated properties are well studied and can be correlated with the resulting characteristic chemical abundances. In Section 2 of this paper we describe the CALIFA survey and how individual H ii regions were extracted from the data-cubes.

The rest of the paper is organised as follows: In Section 3.1 we give the details of the stellar continuum subtraction, emission-line measurement and, in section 3.2, the selection of star-forming H ii regions. The determination of O/H and N/O abundances is described in Section 3.3. **This task was carried out using the model-based semi-empirical code Hii-Chi- mistry. As shown in Pérez-Montero (2014), this method is totally consistent with the direct method when it is compared with H ii regions with available empirical electron temperatures and it is** sensitive to N/O and the ionisation parameter variations. The global relation between O/H and N/O for all H ii regions is presented in Section 4. In Section 5 we describe the calculations of radial chemical variations fittings and the statistical distributions of the resulting slopes and the values at the effective radius. We also analyse the possible correlations between the resulting slopes, the characteristic abundances and other integrated properties of the galaxies, such as luminosity, stellar mass, SFR, colour, morphological type or presence of a bar in Section 6. It is also discussed in Section 7 in detail the case of those objects with a flat or inverted Z gradient. Finally, in Section 8, we summarise our results and present our conclusions.

2. Sample of galaxies and extraction of H II regions

The galaxies observed by CALIFA were selected from the SDSS survey encompassing a wide range of their integrated properties, including mass, luminosity, colours, and morphologies (Walcher et al. 2014), what allows us to insight many of their spatially resolved properties with a statistically significant point of view in the Local Universe ($0.005 < z < 0.03$).

The details of the survey, sample, observational strategy, and reduction are explained in Sánchez et al. (2012a) and García-Benito et al. (2015). All galaxies were observed using PMAS (Roth et al. 2005) in the PPAK configuration (Kelz et al. 2006), covering a hexagonal field of view (FoV) of $74'' \times 64''$ sufficient to map the full optical extent of the galaxies up to two to three disc effective radii. This is possible because of the diameter selection of the sample (Walcher et al. 2014). The observing strategy guarantees a complete coverage of the FoV, with a final pixel size $1''$, corresponding to ≈ 1 kpc at the average zt of the survey.

The CALIFA mother sample consists of 939 galaxies, but for this work we used a sample of 350 objects observed with the gratings V500 and V1200. The observed wavelength range and spectroscopic resolution (3745–7500 Å, $\lambda/\Delta\lambda \approx 850$, for the low-resolution setup and 3650-4800 Å, $\lambda/\Delta\lambda \approx 1500$, for the high resolution setup) are more than sufficient to explore the most prominent ionised gas emission lines, from [O II]λ 3727 to [S II]λ6731, on one hand, and to deblend and subtract the underlying stellar population, on the other (e.g., Sánchez et al. 2012a; Kehrig et al. 2012; Cid Fernandes et al. 2013). The dataset was reduced using version 1.5 of the CALIFA pipeline, whose modifications with respect to the one presented in Sánchez et al. (2012a) are described in detail in García-Benito et al. (2015). In summary, the data fulfill the predicted quality-control requirements with a spectrophotometric accuracy that is better than 15% everywhere within the wavelength range, both absolute and relative with a depth that allows us to detect emission lines in individual H II regions as weak as $\approx 10^{-17}$ erg $\cdot$ s^{-1} $\cdot$ cm^{-2}, and with a signal-to-noise ratio of S/N $\approx$ 3–5, even in the case of [O III] auroral lines presented in Marino et al. (2013).

The final product of the data reduction is a regular-grid datacube, with x and y coordinates that indicate the right ascension and declination of the target and z a common step in wavelength. The CALIFA pipeline also provides the propagated error cube, a proper mask cube of bad pixels, and a prescription of how to handle the errors when performing spatial binning (due to covariance between adjacent pixels after image reconstruction). These datacubes, together with the ancillary data described inWalcher et al. (2014), are the basic starting points of our analysis.

Emission-line regions in the CALIFA galaxies were segregated in the resulting data-cubes and their corresponding spectra were extracted using the semi-automatic routine HIIEXPLORER [1]. The details of this routine are well described in Sánchez et al. (2012b) and Rosales-Ortega et al. (2012), but it is basically based on the assumption that emission-line regions can be found as clumpy and isolated Hα peaks of emission of several arcseconds, which correspond to diameters of a few hundreds of parsecs. The total number of selected emission-line regions from the 350 analysed galaxies following this procedure is 15 757.

[1] Available at http://www.caha.es/sanchez/HII_explorer

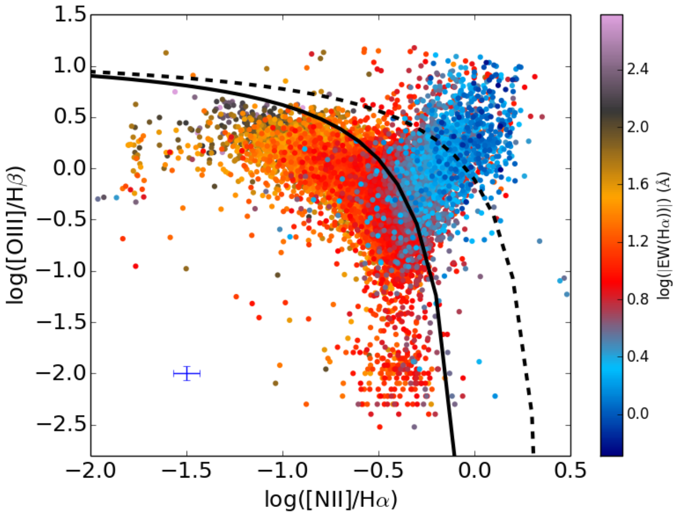

Fig. 1. [O III]/Hβ against [N II]/Hα relation, one of the BPT diagrams, for the 15 757 extracted emission-line regions in the analysed CALIFA galaxies. Colour scale shows the Hα equivalent width. The solid black line represents the empirical curve from Kauffmann et al. (2003) to divide objects ionised by massive stars and by non-thermal processes. The dashed line is the theoretical curve defined by Kewley et al. (2001). The lower left cross indicates the typical associated error in each axes.

3. Analysis of the extracted regions

3.1. Emission-line measurement

The stellar underlying population spectral emission was fitted and removed from the extracted individual spectra of the extracted emission-line regions in order to avoid absorption components of the Balmer emission lines. This continuum was fitted using the program FIT3D v. 2.0 [2] (Sánchez et al. 2006, 2011). This package fits the continuum as a linear combination of several single stellar populations (SSPs) of different ages and Z taken from the MILES project (Vazdekis et al. 2010; Falcón-Barroso et al. 2011). A stellar extinction law by Cardelli et al. (1989) was used in the fitting process, assuming a value of $R_v = 3.1$, a simple dust screen distribution, and that all SSPs have the same dust attenuation.

Once the stellar continuum is subtracted, FIT3D performed a Gaussian function fitting to measure the fluxes of the most prominent emission-lines of the extracted spectra. To reduce the number of free parameters this algorithm forces the systemic velocity and the velocity dispersion to be the same for emission lines produced by the same ion (e.g. [O III] 4959, 5007 ÅÅ) and to apply a multi-component analysis for those blended emission-lines. For the aims of this work, we used [O II] 3727 Å, Hβ, [O III] 5007 Å, Hα, [N II] 6584 Å, and [S II] 6717, 6731 ÅÅ with a signal-to-noise ratio better than 3 as obtained using the above described automatic fitting procedure.

3.2. Selection of star-forming H II regions

The determination of chemical abundances and most of the physical properties in ionised gaseous regions are based on the assumption that the gas is ionised by a spectral energy distribution dominated by very young massive stars during a process of ongoing star formation. Therefore, for the extracted objects in our sample of CALIFA galaxies, it is necessary to separate star-forming regions from other emission-line regions where the main source of ionisation is different (i.e. AGNs, shocks, post-AGB stars).

The most-widely used method based on optical emission lines to detect star-forming regions is based on diagnostic diagrams of emission-line ratios sensitive to the excitation of the gas (e.g. Baldwin et al. 1981 (BPT), Veilleux & Osterbrock 1987). One of these diagrams is the extinction-independent relation between [O III] 5007 ÅHβ and [N II] 6584Å/Hα where different demarcation curves are used to classify the ionising source. In Fig.1 it is shown this diagram for the 15 757 extracted emission-line regions in the 350 analysed CALIFA galaxies and the empirical curve defined by Kauffmann et al. (2003) using SDSS galaxies and the model-based curve defined by Kewley et al. (2001). There is a general consensus that below these two lines, emission-line objects can be considered as star-forming regions while those above both curves are ionised by an AGN or shocks. All regions in that part of the diagram were discarded for the subsequent analysis.

In addition, the regions between these two curves have been proposed to be composite regions, where their ionisation has a mixed origin (i.e. star-formation and nuclear activity) (Kewley et al. 2006), although we can also find pure star-forming regions with an overabundance of nitrogen Pérez-Montero & Contini (2009) or can be ionised by evolved stars (Kehrig et al. 2012). Therefore, to select only star-forming H II regions we also used the criterion described by Cid Fernandes et al. (2011) based on the use of EW(Hα), as a proxy of the weight of the old stellar population. This was measured on the spectra before the subtraction of the underlying stellar population over the continuum. As shown in Fig.1 the distribution of EW(Hα) correlates with the position of the regions in the BPT diagram. In this way, as also carried out by Sánchez et al. (2014), we discarded for our analysis those regions with EW(Hα) > -6 Å. In addition, to ensure that only regions ionised by massive star-formation are used, we took the results from the SSP fitting to select regions with at least a mass fraction of 30% of young stars (i.e. with an age younger than 500 Myr). The number of selected star-forming regions in the 350 analysed CALIFA galaxies using the above criteria is then 8 196.

3.3. Derivation of chemical abundances

Both elemental abundance ratios O/H and N/O were derived in the selected sample of H II regions using the program HII-CHI-MISTRY v.2.0[3] (hereafter HCM) (Pérez-Montero 2014). This method calculates these abundance ratios and the ionisation parameter (log$U$) as the averages and standard deviations of the $1/\chi^2$-weighted distributions of the input conditions in a large grid of photoionisation models calculated with CLOUDY v. 13.01 Ferland et al. (2013). The grid of models cover a wide range in the space of O/H ([6.9,9.1] in steps of 0.1 dex), N/O ([-2.0,.0] in steps of 0.125 dex) and log$U$ ([-4.0,-1.5] in steps of 0.25 dex). However, to avoid the clustering of the resulting quantities around the discrete values of the grid, we calculated linear interpolations both in the O/H and the N/O axis improving the resolution up to 0.02 dex and 0.025 dex respectively.

The $1/\chi^2$ weights are calculated as the quadratic differences between certain observed emission-line ratios and the predictions made for the same ratios in each model of the grid. The observational input consists of the reddening-corrected relative-to-Hβ fluxes of [O II] 3727 Å, [O III] 4363, 5007 ÅÅ, [N II] 6584

[2] Available at http://www.astroscu.unam.mx/~sfsanchez/FIT3D/index.html
[3] Available at http://www.iaa.es/~epm/HII-CHI-mistry.html

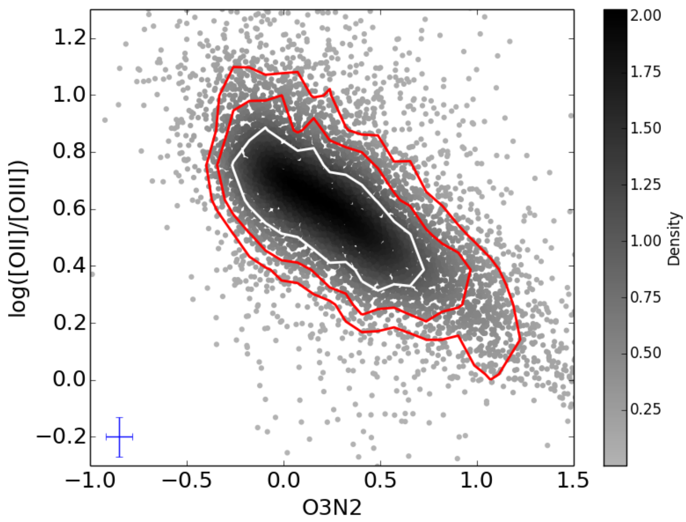

Fig. 2. Relation between the index O3N2, tracer of Z and the emission line ratio [O II]/[O III], tracer of the excitation, for those selected star-forming regions for which [O II] lines were used for the calculation of chemical abundances. Density of points over the mean value are represented according to the colour bar. White solid line represents the 1σ contour, while red lines represent 2σ and 3σ contours. The left lower cross indicates the typical errors of the two ratios.

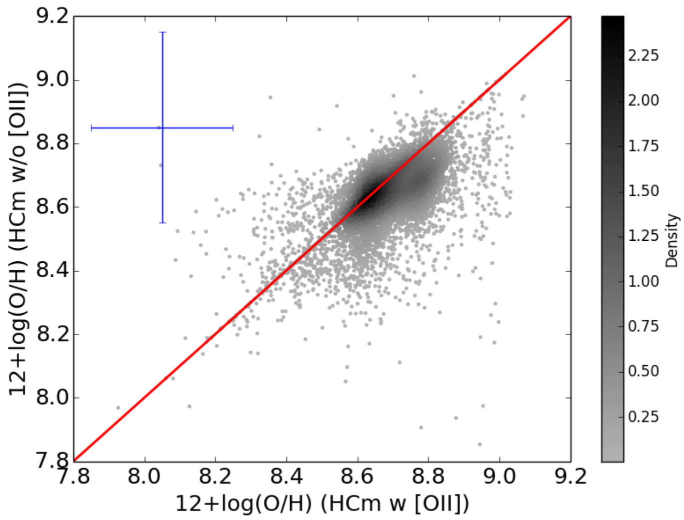

Fig. 3. Comparison between the O/H abundances derived from HCM with and without taking [O II] emission lines. We only represent the H II regions of the sample whose O/H uncertainty is reduced when [O II] is considered. Density of points over the mean value are represented according to the colour bar. The red solid line represents the 1:1 relation. Upper left cross represents the standard deviation of both methods in relation to the direct method as done by Pérez-Montero (2014).

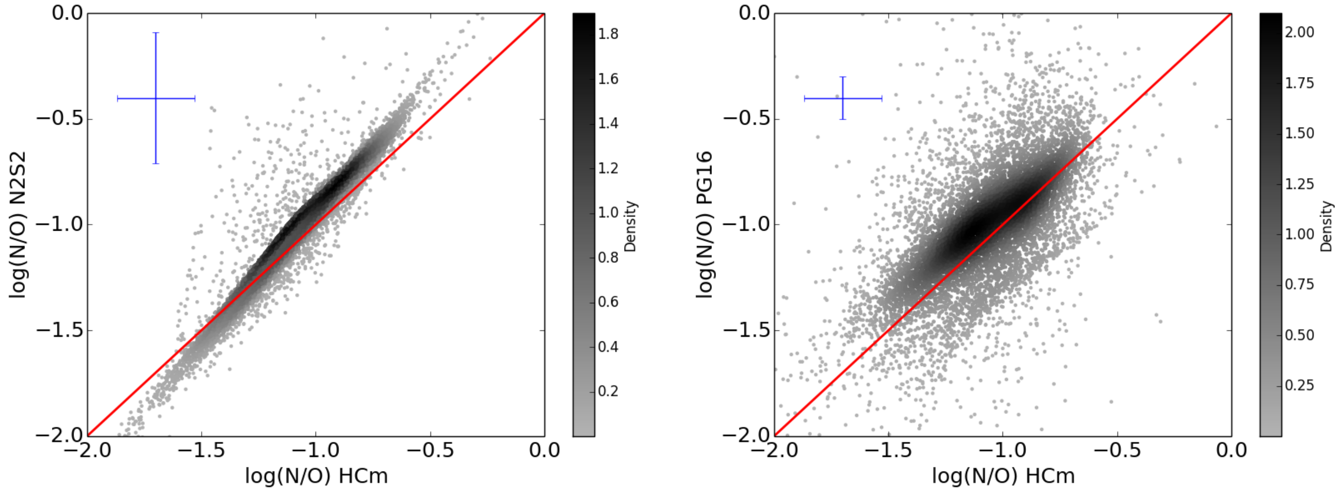

Fig. 4. Comparison between N/O derived from HCm **and from different strong-line methods. At left, for all selected H ii regions, with the N2S2 parameter calibrated by Pérez-Montero & Contini (2009) and. At right with the calibration given by Pilyugin & Grebel (2016) based on [N ii] and [O ii] emission lines** for those regions whose [O ii] lines were used. Density of points over the mean value are represented according to the colour bar. The red solid line represents the 1:1 relation. Upper left crosses represent the standard deviation of the residuals to the direct method as done by Pérez-Montero & Contini (2009) and Pérez-Montero (2014).

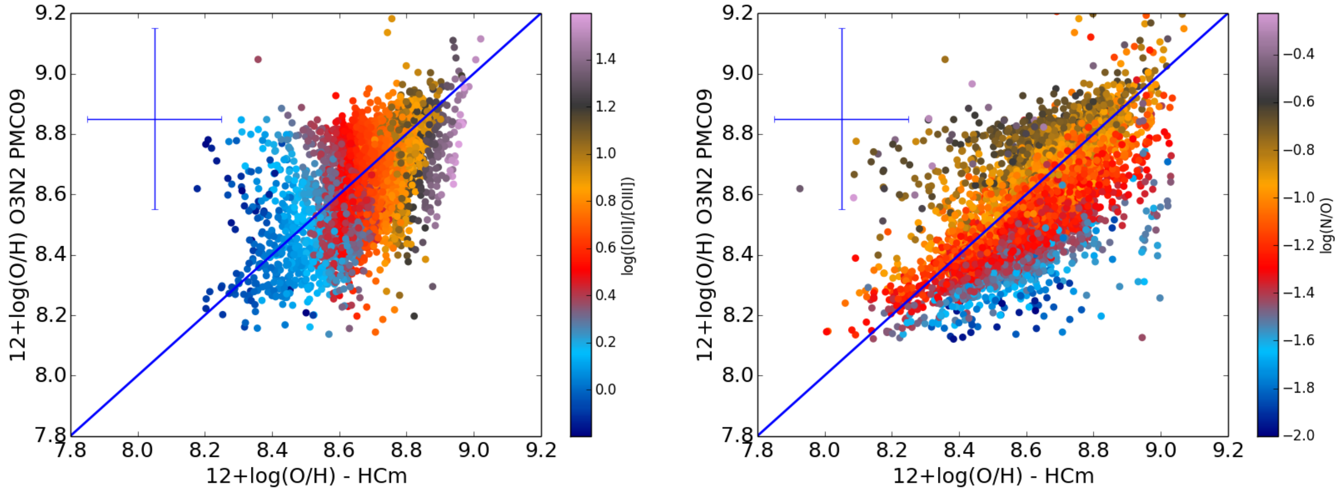

Fig. 5. Comparison between O/H derived from HCm and from the empirical calibration of the O3N2 parameter given by Pérez-Montero & Contini (2009). The **blue** solid lines represent the 1:1 relation. Left panel has a colour scale for the [O ii]/[O iii] ratio and right panel for N/O. **Note that for the sake of consistency the number of points in left panel is lower because [O ii] lines were not used for the derivation of O/H.** Upper left crosses represent the standard deviations of the residuals to the direct method of both methods as compared to the direct method done by Pérez-Montero & Contini (2009) and Pérez-Montero (2014).

Å, and [S ii] 6717+6731 ÅÅ. The extinction correction of all lines was applied comparing the observed Hα/Hβ flux ratio with the theoretical value predicted by Storey & Hummer (1995) for standard conditions of density and temperature (i.e. Hα/Hβ = 2.86 for $T_e = 10^4$ K and $n_e = 10^2$ cm^{-3}) and assuming an extinction law by Cardelli et al. (1989) with $R_v = 3.1$. We checked that the temperature and density variation across the analysed H ii regions introduces an additional uncertainty in the extinction correction much lower than the uncertainties associated to the emission-line measurements.

The analysis performed by Pérez-Montero (2014) shows that when the chemical abundances derived using hcm are compared with the abundances derived using the direct method in a sample of H ii regions and galaxies with a measurement of their electron temperatures, the agreement is much better than the associated errors. This agreement is also found even though the models use only stellar energy distributions of massive clusters from popstar Mollá et al. (2009) with a single age (1 Myr).

Using HCm to derive both O/H and N/O values in H ii regions has three important advantages over other strong-line methods, whether they have been empirically or theoretically calibrated. Firstly, it derives N/O as a first step using appropriate emission-line ratios (i.e. N2O2, N2S2, Pérez-Montero & Contini 2009), allowing the use of [N ii] emission lines to calculate O/H without any prior assumption on the O/H-N/O relation. Secondly, the use of models allows us to obtain **consistent** chemical abundances in a Z regime that cannot be properly calibrated using the direct method (i.e. oversolar abundances) what makes this method especially useful for the chemical study of H ii regions in spiral discs. Finally, HCm leads to values of the abundances consistent with the direct method regardless of the set of emission lines taken as observed input, instead of using different strong-line methods, possibly calibrated in different ways, for different available emission lines.

Unfortunately, in barely any of the selected H ii regions of our CALIFA sample the auroral [O iii] 4363 Å, **needed to calculate electron temperatures,** was measured with enough signal-to-noise. Only for 16 H ii regions this line could be measured with confidence (Marino et al. 2013). For these regions, the agreement between the abundances derived from the direct method and the abundances derived from HCm is better than the derived errors. For the rest of the sample, in absence of the [O iii] auroral line, HCm **uses a limited grid of models empirically constrained to provide chemical abundances consistent with the direct method for the sample of H ii regions with electron temperatures described in Pérez-Montero (2014).** In this way, it is assumed an empirical law between O/H and log$U$ (i.e. higher log$U$ values for lower O/H and vieversa). This O/H-log$U$ relation has been already observed in different samples of H ii regions (e.g. Evans & Dopita 1985; Dopita & Evans 1986) and could be the effect of the use of a biased sample or an evolutionary sequence for the empirical calibration of most strong-line methods. This assumption is well justified in the case of our sample as can be seen in Fig.2, where it is represented the emission-line ratio [O ii]/[O iii], which can be used as an indicator of the excitation of the ionised gas (e.g. Pérez-Montero & Díaz 2005), with the O3N2 parameter (O3N2 = log([O iii]/Hβ·Hα/[N ii])), which in metal-rich objects, correlates with Z (e.g. Alloin et al. 1979). There is a clear trend to find lower values of [O ii]/[O iii] (high log$U$) for high O3N2 (i.e. low O/H) and viceversa. Despite the assumed Z-log$U$ in the models, HCm allows a certain variation of log$U$ for each value of O/H, **according to the observed relation for H ii regions with electron temperatures in Pérez-Montero (2014) and in agreement with** some expected variation of log$U$ across galactic discs (see Ho et al. 2015) or the hardening of the ionising radiation (Pérez-Montero & Vílchez 2009).

Using this constrained grid of models, the uncertainty in the final results is however higher than with the presence of the [O iii] auroral line. As associated error in each H ii region we considered the following quadratic addition:

$$\sigma^2_{HII} = \sigma^2_{HCm} + \sigma^2_g + \sigma^2_{res} \tag{1}$$

where σ_{HCm} is the standard deviation of the resulting distribution of abundances derived by HCm, σ_g is the improved interpolated resolution of the grid of models (i.e. 0.02 dex for O/H and 0.025 dex for N/O), and σ_{res} is the average residual with the sample of objects with abundances derived using the direct method **reported by Pérez-Montero (2014) using a sample of H ii regions with measured electron temperatures** (i.e. 0.22 dex for O/H and 0.16 dex for N/O) in absence of [O iii] 4363Åin the whole range.

Although all optical strong lines required by HCm **were measured in all objects, the [O ii] lines were not used for the calculation of the abundances in all of them (in a 29% of the objects). When the standard deviation of the $1/\chi^2$-weighted model-based abundances were lower without [O ii] these were ruled out in order to reduce the resulting uncertainties (i.e. the [O ii] fluxes can be more uncertain due to a more critical flux calibration in the blue part of the spectrum and to a larger wavelength baseline for reddening corrections). A comparison between the O/H abundances derived by our method with and without [O ii] for those H ii regions whose [O ii] were used is shown in Fig.3. The mean residual is 0.04 dex, much lower than the reported errors, sot his does not affect to the results of this work.**

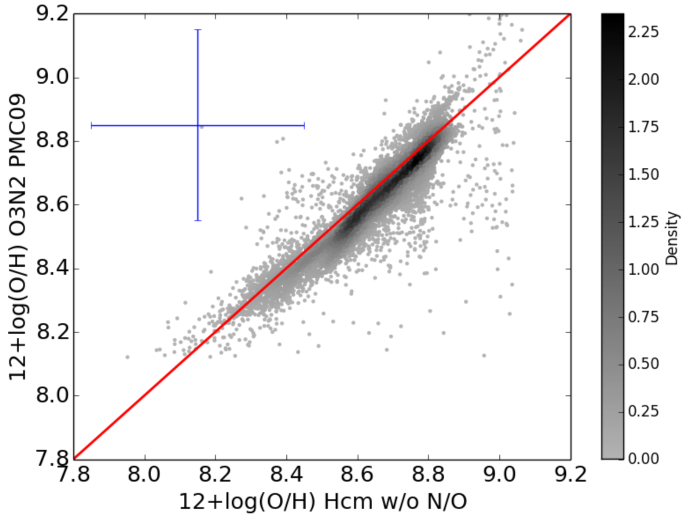

Fig. 6. Comparison between the O/H abundances derived from HCm with the empirical calibration of the O3N2 parameter given by Pérez-Montero & Contini (2009). In this case HCm O/H values were calculated without a previous determination of N/O, but assuming the expected O/H-N/O relation. Density of points over the mean value are represented according to the colour bar. The red solid line represents the 1:1 relation. Upper left cross represents the standard deviations of the residuals of both methods as compared to the direct method done by Pérez-Montero & Contini (2009) and Pérez-Montero (2014).

A direct comparison between the chemical abundances obtained from HCm **and the direct method cannot be established as the electron temperature cannot be measured in almost any H ii regions of the CALIFA sample. However, we compare our results with some other strong-line methods calibrated with the direct method sample. In left panel of Fig.4 it can be seen the comparisons between the N/O obtained from** HCm **with the N/O from the calibration by Pérez-Montero & Contini (2009) of the N2S2 parameter (=log([N ii]/[S ii])) for all the selected H ii regions. At right it is shown the comparison with the N/O from the calibration by Pilyugin & Grebel (2016) based on [N ii] and [O ii] lines only for those objects whose [O ii] lines were used in the** HCm **calculations. In both cases the average of the residuals is much lower than the reported associated uncertainty (i.e. 0.05 dex in both cases), but the standard deviation of these residuals results much lower for N2S2 (0.10 dex) than for the method based on [N ii]/[O ii] calibrated by Pilyugin & Grebel (2016) (0.25 dex).**

Regarding O/H, in order to examine the impact of considering a free O/H-N/O relation in the models as compared with other methods empirically calibrated, we show in Fig.5 the comparison for the selected CALIFA star-forming regions between the O/H derived by HCm **and the empirical calibrations of the O3N2 parameter given by Pérez-Montero & Contini (2009), valid for O/H $\gtrsim$ 8.1. There is not a large systematic offset between the two methods (i.e. the average of the residuals is 0.04 dex) and the dispersion, calculated as the standard deviation of the residuals, is 0.11 dex. To explore the origin of this dispersion we include in both panels of the figure a colour scale representing other quantities. In**

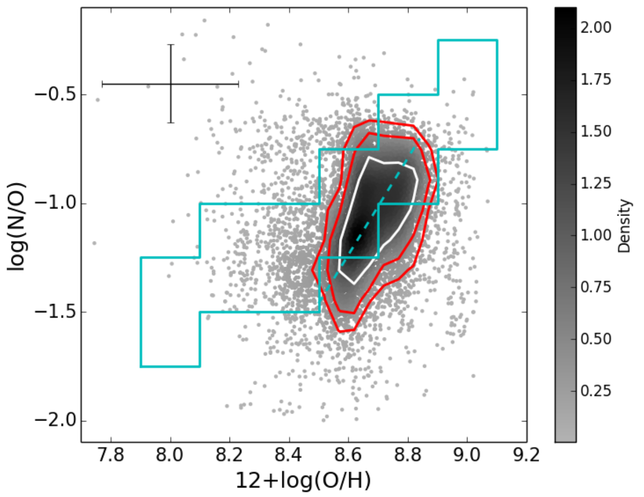

Fig. 7. Relation between O/H and N/O as derived from HCm for all the star-forming H ii regions analysed in the CALIFA sample. Density of points over the mean value are coded by the colours. The solid lines represent the 1σ (white), 2σ, and 3σ (red) contours, while the dashed line shows the linear fitting obtained in the lower panel of Fig.8. Finally, the cyan solid line encompasses the space of models used by HCm to calculate O/H without a previous determination of N/O, taken from the position of objects with a direct chemical abundance in Pérez-Montero (2014). The upper cross represent the typical errors associated with the derivation of abundances using HCm.

left panel, only for those H ii regions whose [O ii] lines were used for the abundance calculation, the emission line ratio [O ii]/[O iii], tracer of the gas excitation, As in the case of Fig. 2 there is a clear trend to find higher excitation for lowerZ. However, there is not any clear indication that the dispersion can be owing to the excitation. On the other hand, in the right panel, the colour scale indicates the N/O ratio. As can be seen the agreement is better for lower Z when N/O is lower, and for higher O/H when N/O is higher. Other combinations of O/H and N/O in the same plane leads to larger deviations of the 1:1 relation producing the observed dispersion.

In Fig.6 we show a similar comparison with O3N2 as calibrated by Pérez-Montero & Contini (2009) but, in this case, the O/H abundances derived using HCm are derived used a grid of models assuming the expected relation between O/H and N/O (i.e. in the regime of secondary production of N, N/O grows with O/H, see right panel of Fig.3 in Pérez-Montero 2014). In this case, the dispersion is very little (i.e. the standard deviation of the residuals is reduced to 0.05 dex). Since most of the objects with electron temperature used to calibrate strong-line methods follow the above typical O/H-N/O relation, the agreement is good when it is assumed. However, as in the case of our sample of CALIFA star-forming regions, the dispersion is enhanced as a consequence of a uncertain N/O value, if it is not previously determined.

4. O/H-N/O for individual H ii regions

The relation between O/H and N/O gives clues about the chemical evolution of the sites where the ionised gas is observed. As O is a primary element it is mainly ejected to the ISM by massive stars. On the contrary, N can have either a primary or a secondary origin. This last regime dominates the production of N in metal-rich H ii regions, as it is produced via the CNO cycle in less massive stars. It is thus expected that N/O correlates with O/H for the H ii regions of the spiral discs.

In Fig.7 it is shown the relation between O/H and N/O calculated using HCm as described above for the 8 196 star-forming regions selected among the 350 analysed CALIFA galaxies. As can be seen there is a trend to find a growing N/O for growing O/H as corresponds to a regime of secondary production of N in metal-rich objects.

We can compare the average position in the O/H-N/O plot of the CALIFA star-forming regions analysed in this work with the line enclosing the regions and galaxies analysed in Pérez-Montero (2014) with electron temperatures and whose O/H and N/O abundances are also derived using HCm by Pérez-Montero (2014) to constrain the grid of models used when a previous N/O determination is not possible. We see that the slope is much higher for the CALIFA regions and that the sample presents much lower values of N/O for lower O/H values. At a same time it can be seen that the relation between O/H and N/O shows a large dispersion. A given dispersion is also found with theoretical models as due to the different efficiencies of SFR in the different regions or galaxies as Mollá et al. (2006) found. In that work the dispersion for the last time step calculated for their models is shown in their Fig.8 around the fitting given for those results. However, the dispersion found with our data seems larger than that one expected as due to different star formation efficiencies It is, however, necessary to take into account that the time evolution also plays a role. As it is seen in Fig.9 from Mollá et al. (2006), different regions or galaxies evolve differently in the plane O/H-N/O, showing steeper tracks when the region/galaxy has higher efficiencies as other with low values which show flat evolutionary tracks. Therefore, the data found below the region of the plane shown by the 1 sigma contours have probably high-medium efficiencies to form stars but are less evolved than the ones in the "standard" locus; while data above are probably regions with low efficiencies.

Besides, the gas interchange between a galaxy and the surrounding IGM, or between different parts of a galaxy, has a very different influence on O/H and the ratio between the abundances of a primary and a secondary element (Edmunds 1990), so the dispersion in the O/H-N/O diagram tends to be larger when gas flows exist in the galaxies.

On the other hand, this plot illustrates the importance of the determination of N/O for the chemical analysis in spiral galaxies. Firstly, as N/O does not follow the expected trend in its relation with O/H and presents a large dispersion, all O/H determinations based on [N ii] lines can lead to wrong results (Pérez-Montero & Contini 2009) and, secondly, the range of variation in this sample is almost three times larger in logarithmic scale for N/O ($\approx$ [-1.8,-0.5]) than for O/H ($\approx$ [8.4-8.9]). Besides, in absence of the [O iii] auroral line, the relative error using HCm is better for N/O (0.16 dex) than for O/H (0.22 dex). Thus, the variations of N/O across galactic discs, can yield more accurate results for the determination of spatial chemical variations across galactic discs.

5. Chemical abundance gradients in discs

5.1. Calculation of linear fittings

By considering the resulting HCm O/H and N/O abundance ratios and the de-projected radial distances of the corresponding selected star-forming regions, in our sample of 350 CALIFA galaxies, robust error-weighted linear fittings were performed.

The analysis was made at all de-projected galactocentric distances normalised to the effective radius. The description about

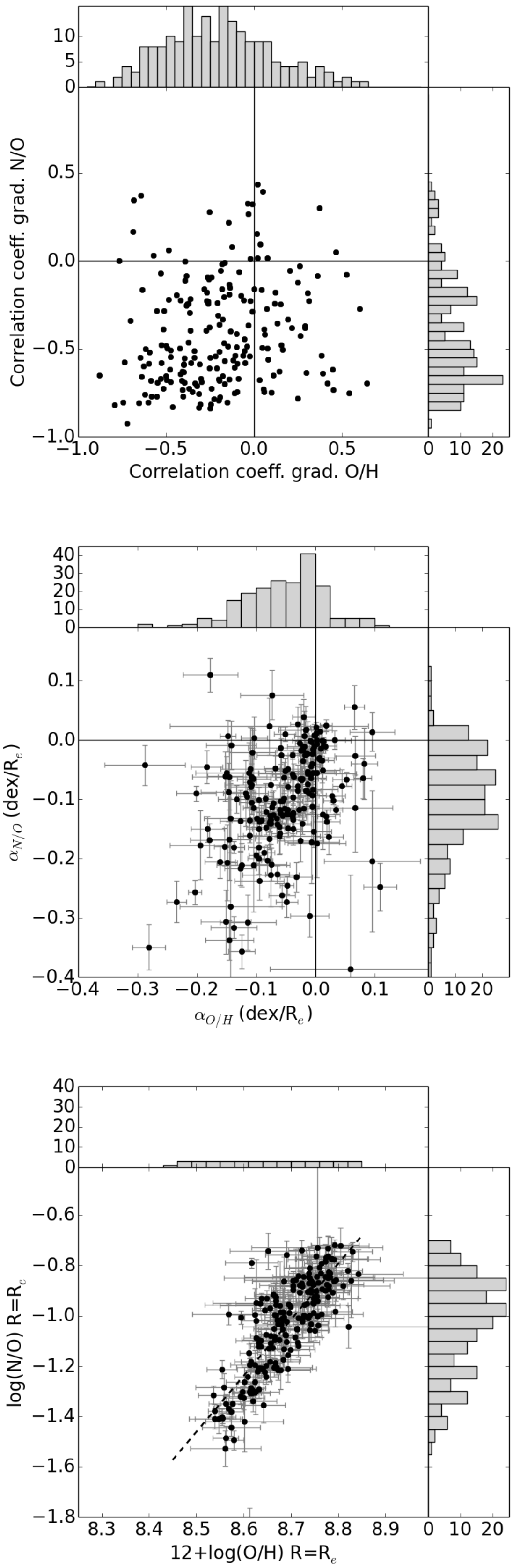

Fig. 8. Histograms and relations of the properties derived from the linear fittings through the radial scale both for O/H and N/O in those galaxy discs of the CALIFA sample with enough star-forming H ii regions. From top to bottom: correlation coefficient, slope of the gradient, and predicted value at the effective radius of the galaxy.

the measurement of the effective radius in each object is given in Sánchez et al. (2014). Only those galaxies with 10 or more selected H ii regions were considered for the subsequent statistical analysis of the sample. We checked in our results the impact of also performing linear fittings over the median values of both O/H and N/O in different radial bins to avoid a oversampling effect in certain radial positions, but we did not find noticeable variations in our results (e.g. the average O/H slopes changes in less than 0.01 dex/R$_e$). In the last section, we present an analysis of the incidence in the results of the very well-known deviations from a strictly linear radial variation of the chemical abundances (i.e. decrease in central positions or flattening at the outermost H ii regions). **We also checked to what extent the calculation of abundances without [O ii] emission lines in ≈ 30% of the H ii regions can affect our results, but these are not localised in specific radial positions and/or galaxies, so the average slopes change in less than 0.01 dex/R$_e$.**

In addition, to rule out environmental effects between the processes that can shape the abundance gradient in galaxies, we did not consider those galaxies with some level of interaction as determined from the visual inspection of their optical images. More details on the interaction stage of each CALIFA galaxy are given in Barrera-Ballesteros et al. (2015).

This leaves the total number of analysed galaxies in 201. The list of non-interacting galaxies with at least 10 selected H ii regions, with their effective radii, inclinations, resulting slopes in dex/R_e, and the values at the effective radius both for O/H and N/O with their corresponding errors can be seen in Table 1.

5.2. Properties of the resulting fittings

In this subsection we analyse the statistical properties of the distributions of the resulting chemical abundance variations across the galactocentric de-projected distances normalized to the effective radius in the 201 CALIFA non-interacting galaxies with 10 or more selected star-forming H ii regions.

In the upper panel of Fig.8 we show the resulting distributions and the relation between the correlation coefficients of the linear fittings to O/H and to N/O. It can be seen that most of the galaxies present both for O/H and N/O a negative coefficient, consistent with the classical idea that spiral galaxies have larger abundances in their inner parts and lower values at larger galactocentric distances. Accepting that the production of N for the metal content of these regions is mostly secondary, it is expected that we also find a negative correlation coefficient for N/O in most of the spiral galaxies. However we also see that a non-negligible fraction of the galaxies present a positive value of this coefficient and that a large dispersion exists between O/H and N/O, in agreement with the large dispersion found for individual H ii regions of the sample seen in Fig.7.

In the middle panel of Fig.8 it can be seen the distributions and relation for the O/H and N/O slopes of the resulting linear fittings, normalised to the corresponding effective radii. Most of the galaxies present a negative gradient both for O/H and N/O. However there is a large dispersion in the corresponding distributions with standard deviations of the same order than the average slopes, which are $\alpha_{O/H}$ = -0.053 ± 0.068 and $\alpha_{N/O}$ = -0.104 ± 0.096.

To evaluate if this large variation is a consequence of statistical fluctuations around a normal distribution, we performed a Lilliefors test. In this test the null hypothesis is that the sample comes from a Gaussian distribution and this cannot be rejected if the significance p-value is larger than 0.1. The resulting p-values are 0.034 for O/H and 0.001 for N/O so, apparently, the queue

Table 1. List of the analysed CALIFA galaxies with their effective radii, inclinations, and the number of H ii regions used to calculate their O/H and N/O slopes and the values at the effective radius of the gradients.

Galaxy[a]	R_e (kpc)	i (°)	H ii regions	$\alpha_{O/H}$ (dex/R_e)	12+log(O/H) (at R_e)	$\alpha_{N/O}$ (dex/R_e)	log(N/O) (at R_e)
ESO539-G014	-0.17 ± 2.3	90	10	-0.006 ± 0.046	8.602 ± 0.083	-0.172 ± 0.070	-1.420 ± 0.120
IC0159	0.19 ± 0.2	40	41	-0.053 ± 0.013	8.632 ± 0.020	-0.064 ± 0.026	-1.207 ± 0.042
IC0480	-0.02 ± 0.5	87	20	0.003 ± 0.000	8.632 ± 0.009	0.000 ± 0.002	-1.123 ± 0.022
IC0776	-0.54 ± 0.3	57	39	0.011 ± 0.049	8.574 ± 0.062	-0.001 ± 0.026	-1.444 ± 0.034
IC0995	-0.61 ± 0.2	84	24	-0.003 ± 0.030	8.619 ± 0.051	-0.155 ± 0.026	-1.337 ± 0.042
IC1151	-0.27 ± 0.2	63	68	-0.028 ± 0.013	8.636 ± 0.019	-0.117 ± 0.012	-1.208 ± 0.020
IC1256	0.24 ± 0.2	55	47	-0.105 ± 0.017	8.734 ± 0.037	-0.115 ± 0.027	-0.950 ± 0.061
IC1528	0.2 ± 0.2	72	70	-0.099 ± 0.011	8.713 ± 0.018	-0.132 ± 0.018	-1.053 ± 0.036
IC2095	-0.7 ± 1.0	90	14	-0.017 ± 0.045	8.562 ± 0.074	0.017 ± 0.039	-1.526 ± 0.070
IC2101	0.52 ± 0.4	90	25	-0.030 ± 0.012	8.666 ± 0.025	0.027 ± 0.029	-1.095 ± 0.072
IC2487	0.24 ± 0.4	84	24	-0.234 ± 0.017	8.755 ± 0.029	-0.273 ± 0.035	-1.001 ± 0.063
IC5309	0.13 ± 0.2	63	25	-0.055 ± 0.021	8.779 ± 0.040	-0.127 ± 0.012	-0.882 ± 0.026
MCG-02-02-040	0.08 ± 0.4	84	22	-0.036 ± 0.012	8.691 ± 0.029	-0.062 ± 0.023	-1.023 ± 0.054
MCG-02-03-015	0.32 ± 0.7	75	12	0.095 ± 0.081	8.676 ± 0.127	-0.204 ± 0.119	-0.959 ± 0.176
MCG-02-51-004	0.54 ± 1.4	72	39	-0.108 ± 0.021	8.699 ± 0.034	-0.105 ± 0.020	-0.965 ± 0.035
NGC0001	0.8 ± 0.1	37	39	-0.026 ± 0.031	8.760 ± 0.064	-0.066 ± 0.061	-0.808 ± 0.121
NGC0023	1.03 ± 0.4	68	27	0.082 ± 0.022	8.715 ± 0.039	-0.040 ± 0.060	-0.842 ± 0.112
NGC0036	0.64 ± 0.4	51	25	-0.105 ± 0.062	8.747 ± 0.094	-0.211 ± 0.079	-0.931 ± 0.125
NGC0165	0.43 ± 0.2	35	28	-0.110 ± 0.050	8.776 ± 0.078	-0.048 ± 0.069	-0.877 ± 0.121
NGC0171	0.02 ± 0.2	52	37	-0.039 ± 0.023	8.691 ± 0.044	-0.130 ± 0.028	-0.758 ± 0.054

[a] The complete table will only be available in electronic form

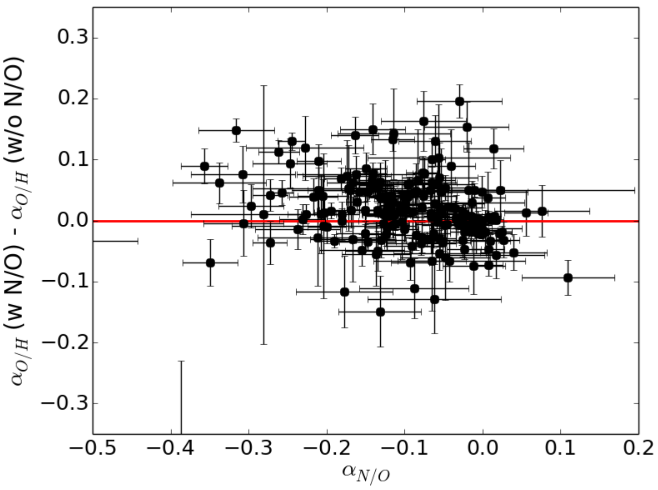

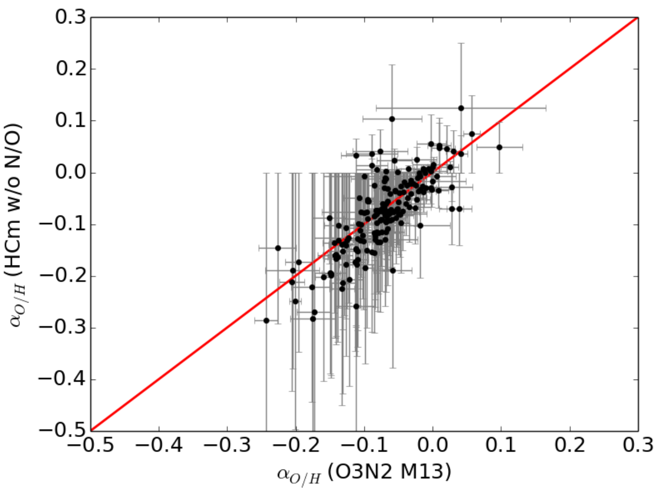

Fig. 9. At left, difference as a function of the N/O slope of the O/H slopes calculated with a previous N/O calculation and the same slopes calculated assuming a given O/H-N/O relation for all the analysed CALIFA galaxies. The red solid line represents the zero value. At right, comparison between the O/H slopes calculated using this last approach with the same slopes calculated using the O3N2 parameter as calibrated by Marino et al. (2013). The red solid line represents the 1:1 relation. All slopes are expressed in dex/R_e

of flat and positive slopes seen in both distributions are not the consequence of a statistical fluctuation.

Although these results confirm the trend to find a negative radial gradient both for O/H and N/O (e.g. Sánchez et al. 2014; Pilyugin et al. 2004), there is a non-negligible fraction of objects that present a flat or even a positive gradient, already observed in the sample of CALIFA galaxies by Sánchez et al. (2014). On the contrary, no objects with inverted O/H or N/O gradients are found by Pilyugin et al. (2004), but the sample analysed there is much smaller. The fraction of these positive gradients are ≈ 19% for O/H and 10% for N/O. However these fractions are reduced to 10% and 4%, respectively, when we only consider those galaxies with a positive slope within the error. The number of galaxies and the average properties of the different sub-samples as a function of the O/H and N/O slopes are shown in Table 2.

Interestingly, the average slope for N/O is more pronounced than for O/H. At same time, the number of objects with an inverted N/O gradient is lower than for O/H. These differences could be caused by two factors: i) N/O is more precise than O/H because the range of variation of N/O for the H ii regions in this sample is much larger with a lower associated mean error (see Fig.7, i.e. the average slope of O/H represents a 5% of the O/H

Table 2. Average slopes and values at the effective radius for the linear fittings of O/H and N/O in the analysed CALIFA galaxies grouped by categorised depending on the sign of the slopes.

	Number	%	$\alpha_{O/H}$ (dex/R$_e$)	12+log(O/H) (at R$_e$)	$\alpha_{N/O}$ (dex/R$_e$)	log(N/O) (at R$_e$)
All	201	100	-0.053 ± 0.068	8.688 ± 0.070	-0.104 ± 0.096	-1.041 ± 0.198
$\alpha_{O/H} < 0$	162	80.6	-0.073 ± 0.057	8.697 ± 0.068	-0.110 ± 0.086	-1.026 ± 0.181
$\alpha_{O/H} < 0$ (1σ)	130	64.7	-0.088 ± 0.054	8.702 ± 0.066	-0.121 ± 0.087	-1.012 ± 0.174
$\alpha_{O/H} > 0$	39	19.4	+0.032 ± 0.032	8.652 ± 0.069	-0.079 ± 0.125	-1.104 ± 0.250
$\alpha_{O/H} > 0$ (1σ)	20	10.0	+0.048 ± 0.033	8.652 ± 0.067	-0.062 ± 0.077	-1.041 ± 0.216
$\alpha_{N/O} < 0$	186	92.5	-0.056 ± 0.068	8.690 ± 0.071	-0.118 ± 0.090	-1.036 ± 0.198
$\alpha_{N/O} < 0$ (1σ)	156	77.6	-0.062 ± 0.068	8.695 ± 0.069	-0.133 ± 0.088	-1.030 ± 0.194
$\alpha_{N/O} > 0$	20	10.0	-0.027 ± 0.065	8.678 ± 0066	+0.025 ± 0.027	-1.075 ± 0.205
$\alpha_{N/O} > 0$ (1σ)	9	4.5	-0.021 ± 0.061	8.674 ± 0.062	+0.041 ± 0.033	-1.107 ± 0.190

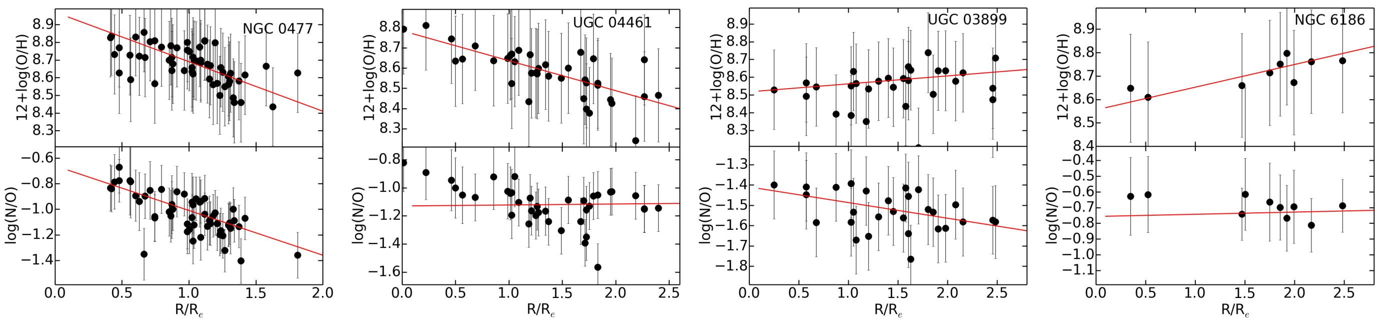

Fig. 10. Four examples of different combinations of slopes in O/H and N/O in the sample of the CALIFA galaxies. From left to right: NGC 0477 presents negative gradients both for O/H and N/O, UGC 04461 shows a negative gradient of O/H, but the N/O gradient is flat. UGC 03899 has positive O/H gradient and a negative N/O one, and finally NGC 6186 shows flat gradients both for O/H and N/O.

range for the CALIFA H ii regions and a 2.5% for N/O), and ii) N/O tends to be unaffected to processes related with hydrodynamical effects caused by the interchange of (un-)processed material between different parts of the galaxies or even with the surrounding IGM. This underlines once again the importance of the determination of N/O in order to calculate chemical abundance gradients.

This N/O dependence can partially explain the lower average slope in this work as compared with Sánchez et al. (2014) and Pilyugin et al. (2004). By using the O/H abundances derived by HCm, but without a previous N/O determination (i.e. using a grid of models assuming a tight O/H-N/O relation as shown by the cyan line in Fig.7), the resulting average slope for the same sample of galaxies is $\alpha_{O/H}$ = -0.069 dex/R$_e$. The difference between the O/H slope derived in a galaxy using N ii] lines when we consider a previous N/O calculation depends on the resulting N/O slope, as can be seen in left panel of Fig.9. This difference is negative for galaxies with a flat or inverted N/O gradient and positive for negative N/O slopes (i.e. when we calculate N/O, the resulting O/H slopes are flatter in those alaxies with a steeper N/O negative gradient). In average, the mean O/H slope is 0.02dex flatter when we consider a previous N/O estimation in the space of the grid of models for this sample. If we compare the O/H slopes derived using this constrained grid of models with the O/H slopes derived using a strong-line method that does not consider any N/O dependence the difference is very little. In right panel of Fig.9 we show a comparison with the slopes obtained from the O3N2 parameter as calibrated by Marino et al. (2013), and the residuals have an average lower than 0.01 dex/R$_e$.

On the other hand, the differences between the behaviours of O/H and N/O radial variations are also evidenced by the not very high correlation between the slopes (Spearman's coefficient, ρ_s = 0.39). Indeed, as it can be seen in Table 2, the average N/O slope for those galaxies with a positive O/H gradient is negative, although flatter than for the whole sample. Similarly, the average O/H slope for those galaxies having a positive N/O gradient is negative although, again, with a flatter value as compared with all galaxies. The lack of a perfect correlation between O/H and N/O gradients is illustrated in Fig.10, where four different combinations of gradient trends for O/H and N/O are shown.

Finally, in the lower panel of Fig.8 it is shown the distributions and scatter plot for the O/H and N/O values at the effective radius as calculated from the robust error-weighted linear fittings. The average values are listed for all galaxies and as a function of the O/H and N/O slopes in Table 2. Contrary to the relation between abundance ratios shown in Fig.7 for individual H ii regions, the dispersion is very low and there is a high correlation coefficient (ρ_s = 0.80, while for individual H ii regions is 0.38) between the characteristic O/H and N/O values. A linear fitting to these points yields the following relation:

$$\log(N/O) = -20.39 + 2.23 \cdot [12 + \log(O/H)]$$

with a standard deviation of the residuals of 0.12 dex. This linear fitting is also plotted in lower panel of Fig.8.

This very good correlation between O/H and N/O values at the effective radius in contrast to the same relation for individual H ii regions or to the slopes of the same gradients, could be the consequence that the typical expected values of Z are not so sensitive to possible internal variations across the discs, but mostly depend on other integrated properties of the galaxies. This idea was already shown by Pilyugin et al. (2004), where a characteristic abundance value for spiral galaxies correlates much better with some of the properties of the discs. According to them this value corresponds to the Z predicted by the linear fitting at 0.4

times the isophotal radius (R_{25}). In our sample of selected CALIFA galaxies the galactocentric distance $0.4 \times R_{25}$ corresponds in average to ≈ 2 times the effective radius, but in what follows, we will consider as typical values of the metal content of the studied galaxies those at the effective radius to study possible correlations between the characteristic O/H and N/O at the effective radius in order to study the relation between these abundances and other integrated properties of the galaxies. This correlation between integrated properties and the fitted radial structure of the spiral galaxies studied in the CALIFA survey has been also observed in the stellar parameters by González Delgado et al. (2015).

6. Correlation with integrated galactic properties

6.1. Relation with luminosity and stellar mass

In this subsection we study to what extent is there a statistical dependence of the slopes or the characteristic abundance ratios with the total luminosity and the stellar mass of the 201 CALIFA galaxies with a derivations of the O/H and N/O radial variations.

In Fig.11 we show the derived slopes and the characteristic values both for O/H and N/O along with the running medians for bins of 25 elements as a function of the integrated absolute magnitude in the SDSS filter g as derived by Walcher et al. (2014) using growth curves. As it can be seen there is a slight trend to find flatter gradients both for O/H and N/O for lower luminosities. This is more evident in the case of N/O although, in both cases, the errors prevent from being totally confident with this result. For the less luminous galaxies of this sample (M_g > -19.5) the mean slope is -0.014 dex/R_e for O/H and -0.055 dex/R_e for N/O, while for the more luminous (M_g < -20.25) the mean slopes are -0.067 for O/H and -0.118 dex/R_e for N/O.

Very similar results are found when we look at the relation with the total stellar mass, which is shown in Fig.12 both for O/H and N/O. The stellar mass derivations for this sample are described in Sánchez et al. (2013). The average slopes for galaxies with $\log(M/M_\odot) < 9.5$ are less prominent both for O/H (-0.019 dex/R_e) and for N/O (-0.061 dex/R_e) than for the rest of the sample. However, no clear trend is seen in this case for the high mass galaxies. When we restrict the sample of galaxies only to those with an inclination lower than 70^o (113 objects) we still see the same trend to find sensibly shallower slopes for low luminosity/mass objects (i.e. for M_g > -19.5, $\alpha_{O/H}$ = -0.028 dex/R_e and $\alpha_{N/O}$ = -0.059 dex/R_e).

Other works (e.g. Sánchez et al. 2014; Ho et al. 2015) have not found any clear correlation between the average slope, of the O/H gradients, once normalized by the effective radius, with the total luminosity or the total stellar mass. Our results point to a trend to find flatter slopes for less luminous and less massive galaxies but it is necessary to improve the statistical significance of the results to confirm this trend.

In lower panels of Fig.11, in the case of the integrated absolute g luminosity, and in Fig.12, for the total stellar mass, we can see the respective relations with the obtained values of O/H and N/O at the effective radii. As it can be seen there are tight and very-low dispersion relations confirming for this sample the known connections between the total luminosity and/or stellar mass of a galaxy with Z content (e.g. Lamareille et al. 2004; Tremonti et al. 2004) and with N/O (Pérez-Montero & Contini 2009; Pérez-Montero et al. 2013). In the case of O/H this result confirms the one obtained by Pilyugin et al. (2004) who find a tighter correlation with luminosity, as a proxy of the stellar mass, and with rotation velocity, as a proxy of the dynamical mass, when a characteristic oxygen abundance value at a specific radial position from a fitting is assumed. This characteristic value was situated at 0.4 times the isophotal radius, instead of using an integrated value of Z.

In our case a quadratic relation can be fitted between the total stellar masses and the O/H values at the effective radius:

$$y_1 = 8.1994 + 0.0.0168 \cdot x - 0.0031 \cdot x^2$$

where x is $\log(M/M_\odot)$ and y_1 is O/H. This fitting has only a standard deviation of the residuals for the 201 studied galaxies of 0.03 dex, much lower than the uncertainty associated to the O/H derivation and the O/H characteristic values in each galaxy.

A similar fitting for N/O at the effective radius yields:

$$y_2 = -8.0611 + 1.1581 \cdot x - 0.0456 \cot x^2$$

where x is $\log(M/M_\odot)$ and y_2 is N/O. For this fitting the standard deviation of the residuals is also of 0.03 dex, much lower than the error associated to N/O derivation and to the characteristic N/O values.

6.2. Relation with present-day star formation and colour

Regarding the relation between the metal content of a galaxy and its total SFR, it has been suggested, for certain samples of galaxies, that, using the integrated emission of star-forming galaxies, there is a dependence between Z and SFR. This dependence points towards lower Z values for higher SFRs in a specific mass bin, reducing the dispersion of the MZR in the so-called fundamental metallicity relation (FMR, e.g. Mannucci et al. 2010; Lara-López et al. 2010). According to Pérez-Montero et al. (2013) from the analysis of SDSS data, the SFR dependence is not observed with N/O, so this could be indicative that the SFR-Z for each mass bin is due to the presence of inflows of metal-poor gas and/or outflows of enriched gas, that do not affect to N/O, but can considerably alter both to SFR and Z.

It is thus interesting to examine if the slopes or the characteristic values of the chemical abundances calculated for the sample of CALIFA galaxies depend on their integrated SFR. The integrated SFR were calculated using the extinction-corrected integrated Hα fluxes following the same procedure as described in Sánchez et al. (2013).

In the upper panels of Fig.13 we see the derived O/H and N/O slopes, with their corresponding running medians, as a function of log SFR. As in the case of stellar mass, there is a very slight, not statistically significant, difference between the O/H slopes of low and high SFR (i.e. $\alpha_{O/H}$ = -0.043 dex/R_e for SFRs lower than the mean value, $10^{0.2}$ $M_\odot$/yr, and -0.062 for higher SFRs). For N/O a similar trend is obtained but the difference between the two bins is lower than 0.01 dex/R_e.

Much more clearly, in the middle panels of the same figures, we see that there is a trend both for O/H and N/O to find higher characteristic values at the effective radius for galaxies with a higher integrated SFR. To check if this relation goes on the contrary sense than the FMR, we examine the relation between SFR and the stellar mass. In left panel of Fig.14 we show this relation for the sample of CALIFA galaxies selected for the analysis of radial gradients. As in the case of the galaxies of the main sequence of star formation Brinchmann et al. (2004), the SFR correlates with the stellar mass of the galaxies, as expected from the fact that larger galaxies have larger gas repositories. Taking the mass-SFR relation obtained from the corresponding running median for this sample, we used the observed MZR and MNOR plotted in Fig. 12 to compare the resulting SFR-O/H or SFR-N/O

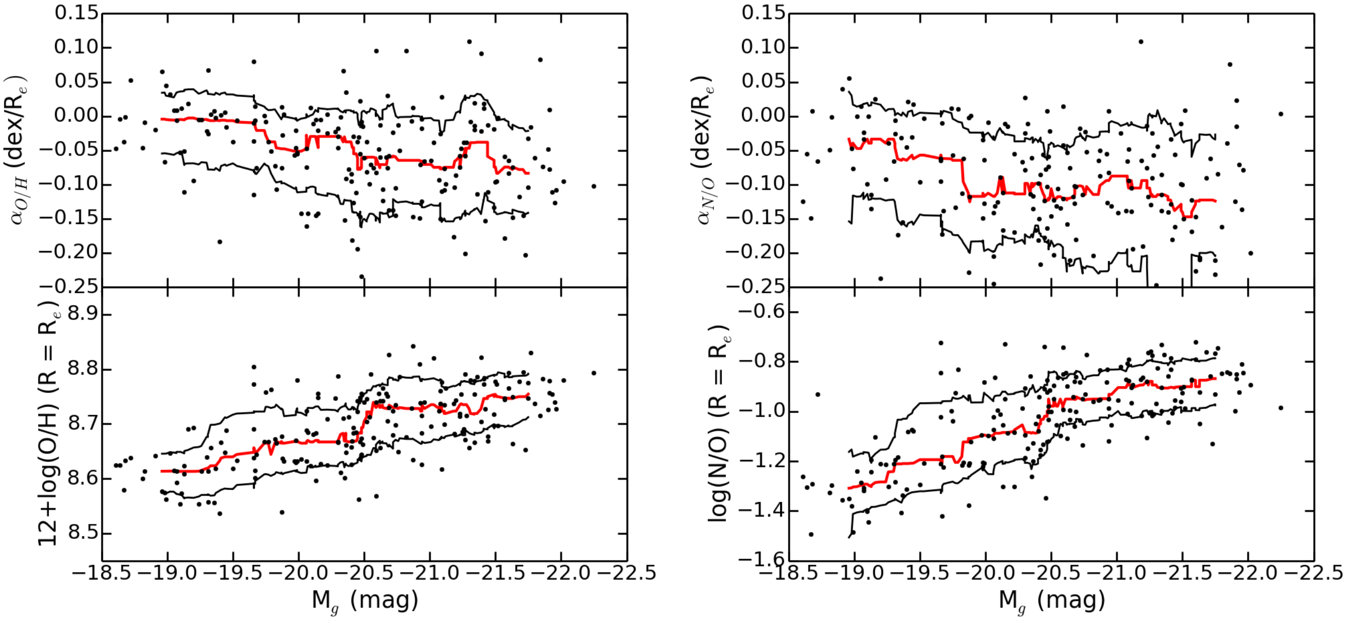

Fig. 11. Relation between the absolute luminosity in the g band and the derived slopes and characteristic values at the effective radius for O/H (left panels) and N/O (right panels). The red solid line represents the Running median for bins of 25 objects, and the black solid lines the 1σ above and below the averages in the same bins.

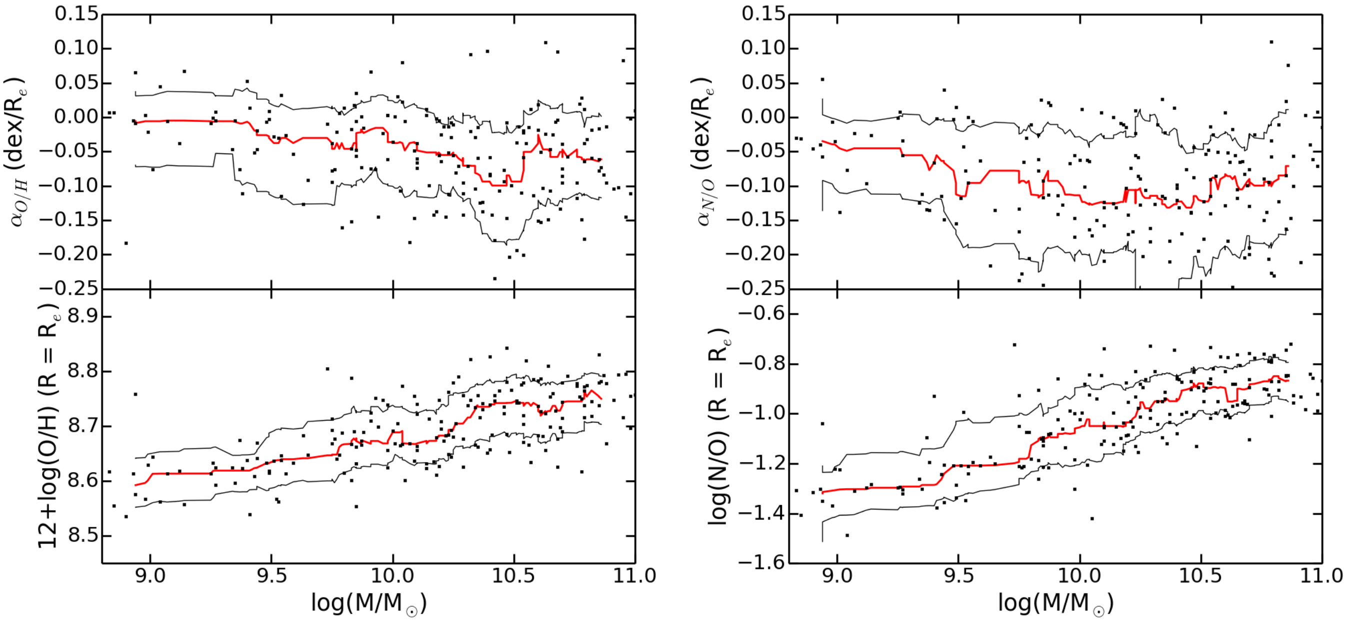

Fig. 12. Relation between the total stellar mass and the derived slopes and characteristic values at the effective radius for O/H (left panels) and N/O (right panels). The red and black solid lines have the same meaning as in Fig. 11.

with the same observed relations. As it can be seen in the lower panels of Fig.13 the residuals between the SFR-O/H (at left) and SFR-N/O (at right) and the same relation considering the observed M-SFR relation are very small. The standard deviations of these residuals are 0.03 dex for both plots, with no mean deviation at any SFR. This M-SFR relation also explains the slight slope difference observed for O/H, as low mass galaxies have, in average, slightly flatter slopes.

We can therefore conclude that no additional dependence between O/H or N/O and SFR is observed for this sample of galaxies, contrary to the results pointing to the existence of the FMR. This agrees with the results in Sánchez et al. (2013) for individual CALIFA H II regions, for which no additional relation between O/H and SFR is found, supporting a scenario of gas recycling faster than gas accretion from inflows or mass loss by outflows.

Although a certain relation between O/H (or N/O) and the SFR is observed for individual H II regions, this is again a consequence of the M-SFR relation. In Fig.15, it can be seen a certain correlation between the O/H of the individual H II regions and their Hα luminosity (ρ_s = 0.17), that is even clearer for N/O (ρ_s = 0.42). These correlations can be explained as due to the stellar mass of the galaxies hosting the H II regions. The average L(Hα) is lower for the less massive galaxies than for the more massive

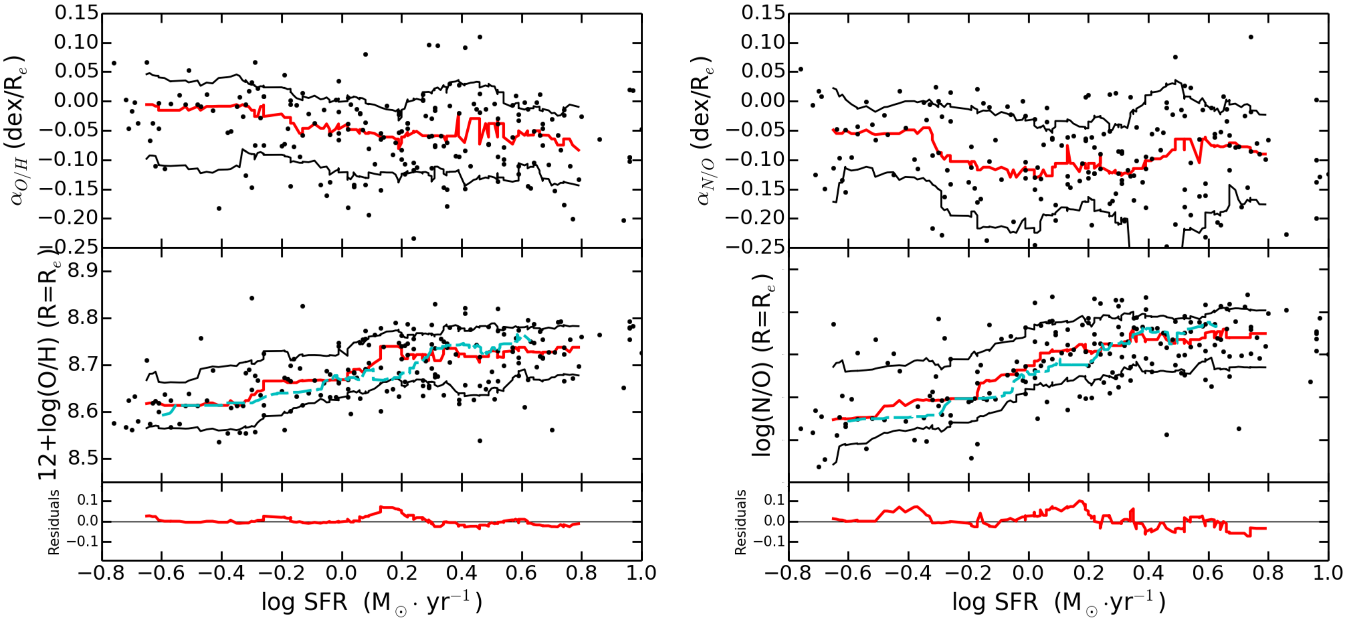

Fig. 13. Relation between the integrated SFR and the derived slopes and characteristic values at the effective radius for O/H (left panels) and N/O (right panels). The red and black solid lines in upper and middle panels have the same meaning as in Fig. 11. In the middle panels, the dashed cyan line represents the running median assuming the observed relation between SFR and stellar mass. In the lower panel it is shown the residuals the red and the cyan running medians.

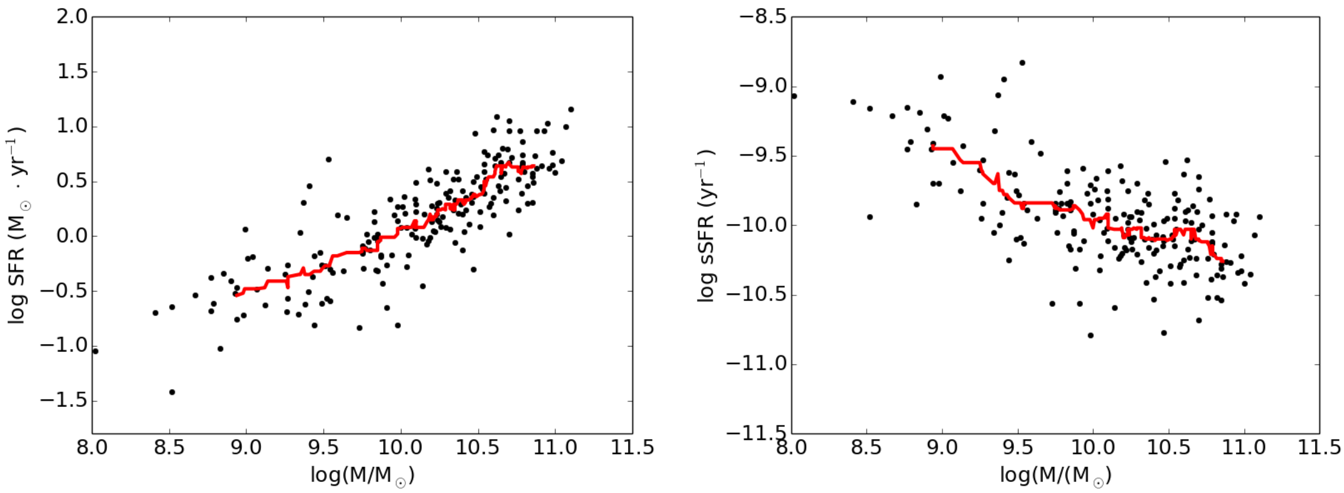

Fig. 14. Relation between the total stellar mass and the present-day integrated SFR (at left) and the sSFR (at right) for the 201 selected spiral non-interacting CALIFA galaxies. The red solid lines represents the running median for bins of 25 objects.

galaxies. The mean L(Hα) = $10^{38.89}$ erg/s for $M_* < 10^{10.22}$ M$_\odot$ and $10^{39.43}$ for higher masses, being M=$10^{10.22}$ M$_\odot$ the median stellar mass of the 201 galaxies with an estimate of the abundance gradient.

Quite similar results are obtained when we analyse the dependence between the slopes of the gradients or the characteristic abundance values with the specific star formation rate (sSFR = SFR/M), which can be considered as an indicator of the ratio between present-day and past SFR. There are also evidences in the literature that for a specific mass bin galaxies with higher sSFR have in average lower *Z* (e.g. Ellison et al. 2008). The resulting median slopes and characteristic values can be seen in Fig.16.

As in the case of the mass or the SFR, a slight trend to find flatter O/H and N/O gradients for galaxies with a lower sSFR is found (i.e. $\alpha_{O/H}$ = -0.029 dex/R$_e$ ($\alpha_{N/O}$ = -0.085) for the bin of sSFR lower than the median ($10^{-9.97}$ yr^{-1} and $\alpha_{O/H}$ = -0.059 dex/R$_e$ ($\alpha_{N/O}$ = -0.105) for the upper sSFR bin.)

Regarding characteristic values, a clear trend to find lower values both for O/H and N/O for higher values of sSFR is seen in the middle panels of the same figure. However, as in the case of SFR, we see that this relation is owing to the previously studied MZR in combination with the relation between mass and sSFR observed in right panel of Fig.14. This sample of galaxies, again, shows in this plot a clear relation as sSFR is lower for galaxies of higher stellar mass. By comparing in lower panels of Fig.13 the relations O/H - sSFR or N/O - sSFR with the running medians of the MZR using the M - sSFR relation, we find that the standard deviation of the residuals is lower than 0.02 dex in both cases.

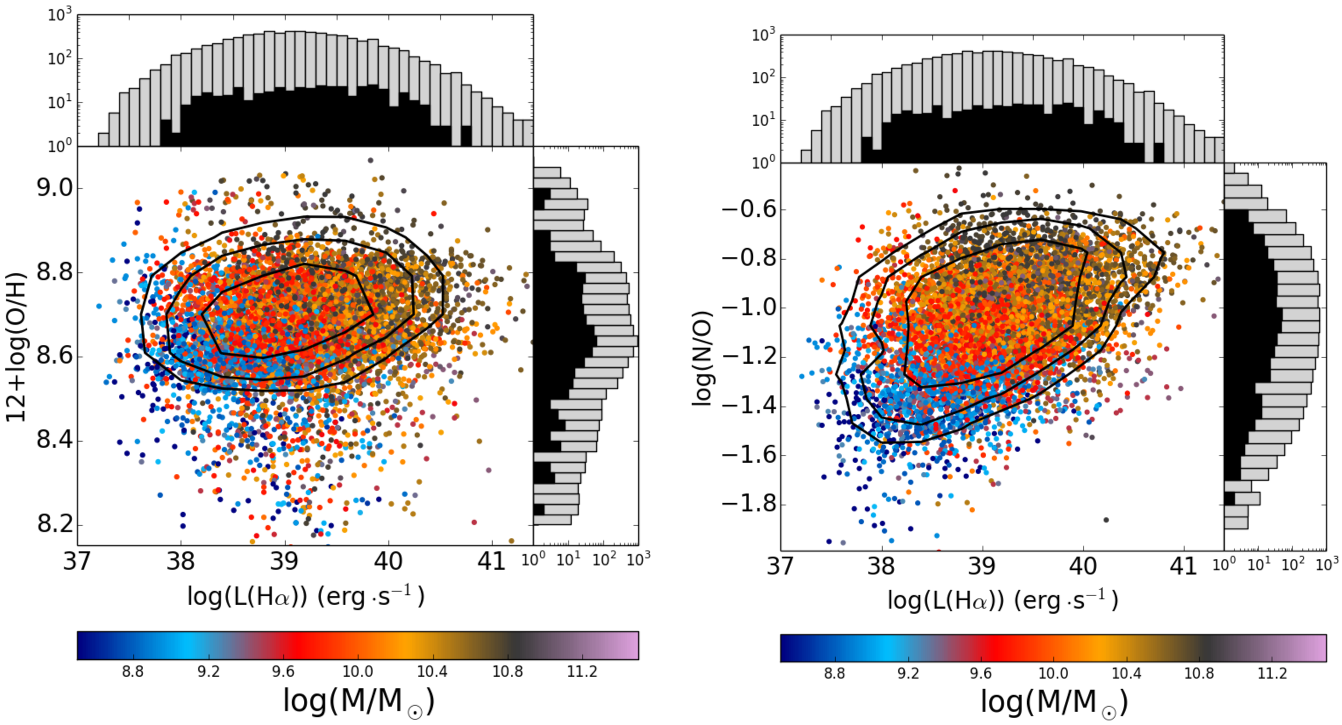

Fig. 15. Relation between the Hα luminosity and O/H, at left, and N/O, at right, for the selected H II regions of the galaxies for which a linear gradient was calculated. The color encodes the total stellar mass of the galaxy where each H II region is situated. The histograms show in logarithmic scales in all axes the distribution for all objects represented in the plot (white bars) and for those H II regions in a galaxy with an inverted gradient (black bars). Colors indicate the density of points and solid lines represent the 1σ, 2σ, and 3σ contours.

The same behaviour between slopes or characteristic values is observed in Fig. 17, where we analyse these quantities as a function of the integrated photometric colours $g - r$ (Walcher et al. 2014), which can be interpreted as a proxy of the relation between on-going and past star formation, as sSFR. In the respective upper panels, no evident relation is found between the O/H and N/O slopes and the integrated colours. On the contrary, in lower panels bluer galaxies tend to have lower abundances and redder objects tend to have higher abundances. Again, as in th case of SFR and sSFR, this result must be interpreted on the light of the MZR and the relations of the colour with stellar mass for this specific non-interacting CALIFA sample with many H II regions. When we assume the observed relation between mass and $g - r$ colour index in the figures, we cannot see significant differences with the observed pattern, what demonstrates that no additional dependence exists between colour and Z or N/O.

The observed empirical relation between colours and masses in this sample goes in the same direction pointed out for the CALIFA sample by González Delgado et al. (2015), who show that in average less massive galaxies are bluer and more massive galaxies are redder. Some works have suggested that a correlation between N/O and the integrated colour can be indicative of the star formation history owing to the delay in the ejection of N to the ISM (e.g. dwarf irregular galaxies, van Zee & Haynes 2006; López-Sánchez & Esteban 2010). However, in our sample, as most of the observed N has a secondary origin, the correlation with colour, is totally understood in terms of the MNOR and the M-sSFR relation.

6.3. Relation with morphological type

In this subsection we analyse the possible link between the calculated slopes and characteristic O/H and N/O values with the morphological type for the 201 galaxies of our CALIFA sample of non-interacting galaxies. The morphological classification was performed by eye, based on independent analysis by members of the CALIFA collaboration and the results are compatible with other photometric indexes, and it is described in detail in Walcher et al. (2014).

The results for the averages of slopes and characteristic abundance values at the effective radius for the different morphological types are listed in Table 3 and are also represented in Fig.18. As can be seen in the respective upper panels, there is a slight trend to find shallower gradients both for O/H and N/O for late-type galaxies ($\alpha_{O/H}$ = -0.018 dex/R$_e$ and $\alpha_{N/O}$ = -0.065 dex/R$_e$ for Sd galaxies). At same time, for O/H there is also a trend to find shallower gradients for early-type galaxies ($\alpha_{O/H}$ = -0.022 dex/R$_e$ in Sa galaxies). This result agrees with the trend found in Sánchez et al. (2014), who found a slightly shallower gradient in average for very early spiral galaxies and also with the results found by Vila-Costas & Edmunds (1992) and Zaritsky et al. (1994) who find steeper gradients in the intermediate-type galaxies. A similar result is found for the slope of the gradient of the stellar properties by González Delgado et al. (2015) in the CALIFA sample.

Regarding the abundance values at the effective radius, considered as characteristic of the metal content of each galaxy, there is an evident decrease of the O/H value, and which is even more evident for N/O, when we move from early to late-type galaxies (i.e. O/H is reduced in 0.14 dex and N/O in 0.35 dex

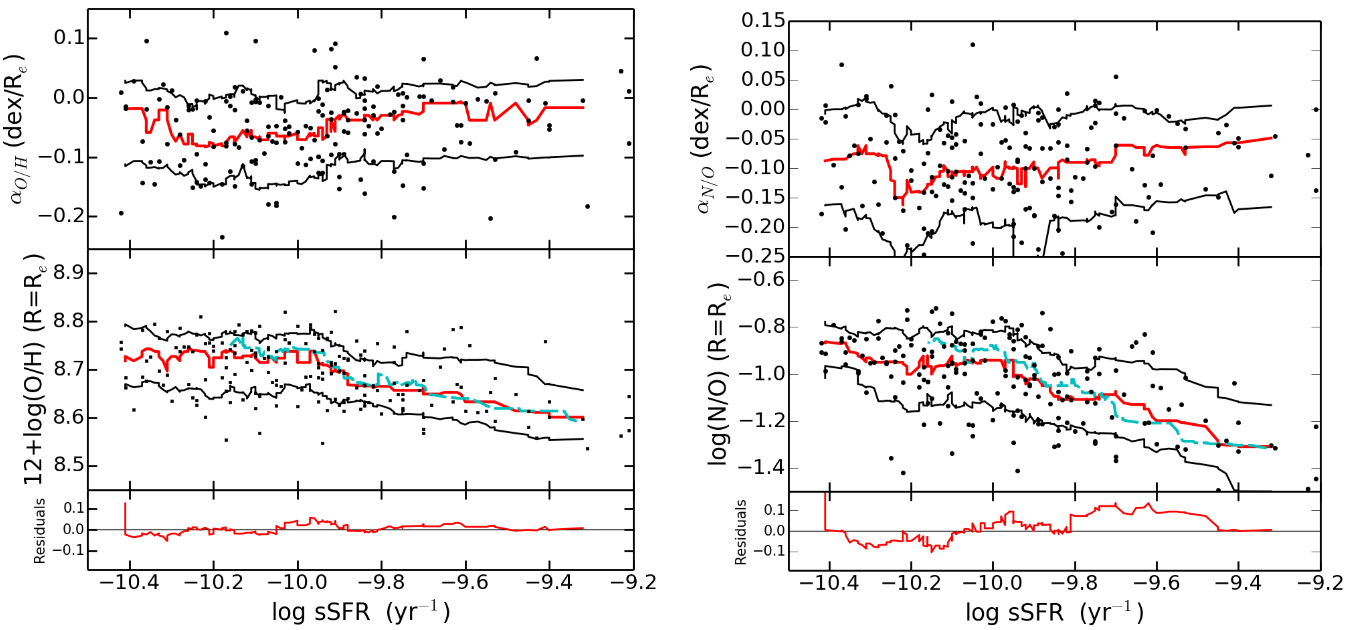

Fig. 16. Relation between the integrated sSFR and the derived slopes and characteristic values at the effective radius for O/H (left panels) and N/O (right panels). The red and black solid lines in upper and middle panels have the same meaning as in Fig. 11. In the middle panels, the dashed cyan line represents the running median assuming the observed relation between SFR and stellar mass. In the lower panel it is shown the residuals the red and the cyan running medians.

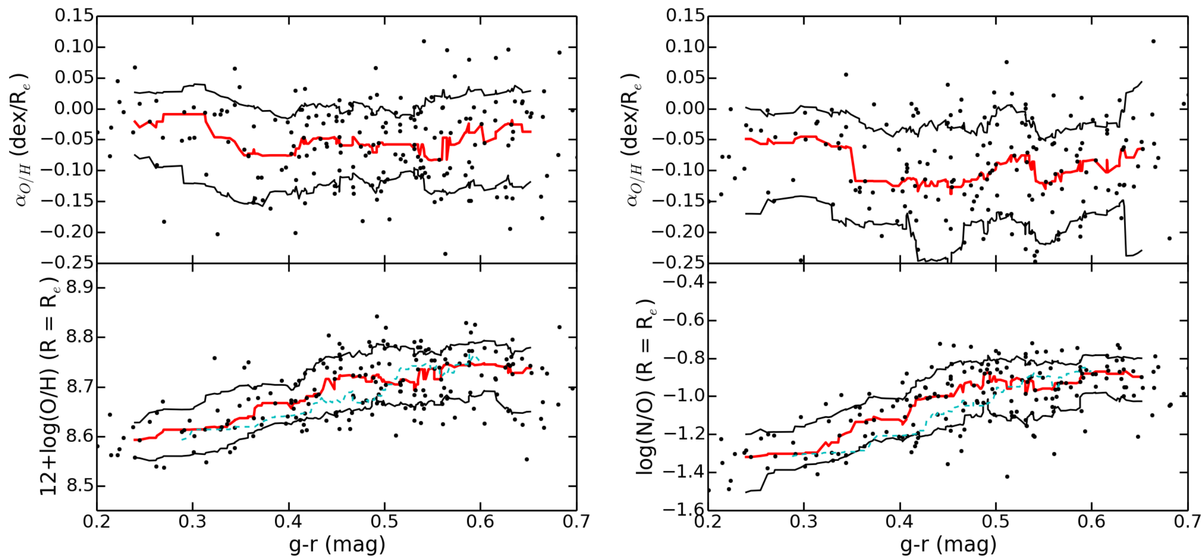

Fig. 17. Relation between the colour index $g - r$ and the derived slopes and the characteristic values at the effective radius for O/H (left panels) and N/O (right panels). The red and black solid lines have the same meaning as in Fig. 11. The dashed cyan lines represents the running median assuming the observed relation between $g - r$ and stellar mass for the same galaxies.

from the early to the late types). This same pattern was already pointed out by Roberts & Haynes (1994).

However, this result must be inspected on the light of the relation between the typical metal content of a galaxy and its stellar mass explored in above subsections. In this sample, there is a bias in the sense that late-type galaxies tend to have lower masses in average than early-type galaxies. In the lower panels of Fig.18 we also show the median values for O/H and N/O at the average stellar mass of each morphological type group. As it can be seen, no apparent difference appears between the expected values at the average stellar mass and the found value at a specific Hubble type (i.e. the mean difference is lower than 0.02 dex both for O/H and N/O).

Then we can conclude that the observed relation between slopes or characteristic values with the morphological types are owing to the combined effect of the MZR or the MNOR and the relation mass-morphological type of this sample. This relation has been also observed for the CALIFA sample of galaxies by González Delgado et al. (2015) by means of the analysis of the spatial distribution of the stellar properties of the galaxies.

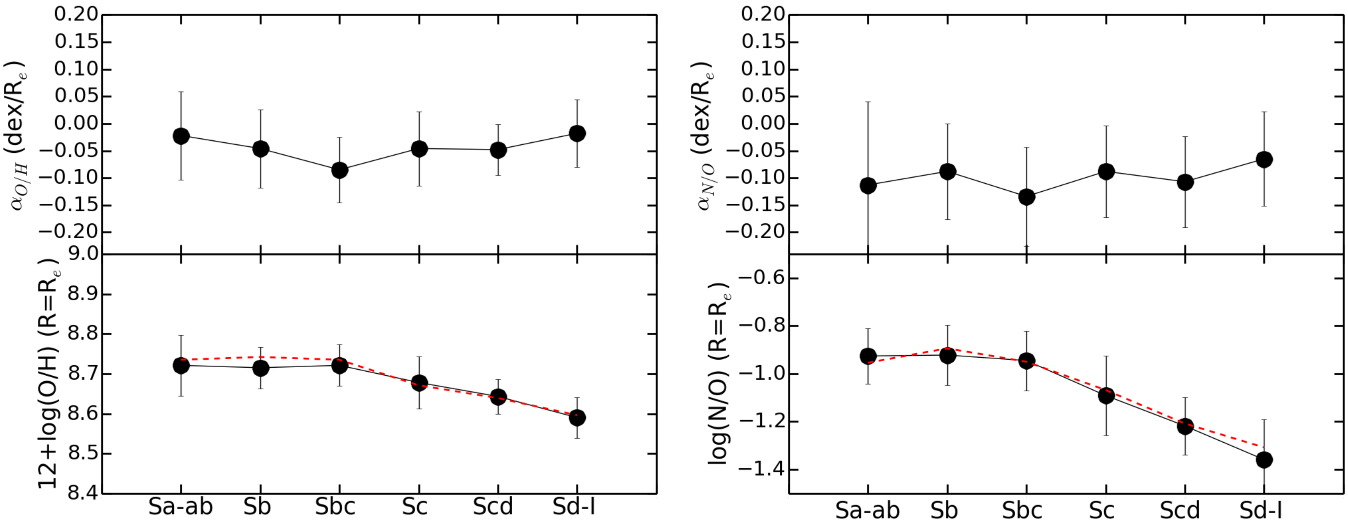

Fig. 18. Average slopes and value at the effective radius of the linear fittings in the non-interacting analysed galaxies as a function of the morphological type for O/H (left panels) and N/O (right panels). The black solid lines join the average points for each morphological types, while the red dashed lines correspond to the average typical abundance ratios found at the average stellar mass of each type.

6.4. Relation with the presence of a bar

It has been proposed that the presence of a bar can be an element important to explain the flattening of gradients of chemical abundances in spiral galaxies. Vila-Costas & Edmunds (1992) and Zaritsky et al. (1994) find this trend in their samples of spiral galaxies and they claim that this could be the consequence of the presence of gas-flows driven by the bars what make the metal distribution to homogenise throughout the discs.

The inspection of our sample for the presence of bars was performed by eye by members of the CALIFA collaboration, and it is described elsewhere in detail in Walcher et al. (2014). Three different groups were defined, following the classical scheme: (A) galaxies with no bar, (AB) galaxies that may have a bar, but it is not clearly visible, and (B) clearly barred galaxies. The visual classification was cross-checked with an automatic search for bars that produced very similar results.

The results for the averages of slopes and characteristic abundance values at the effective radius for the three analysed categories are listed in Table 3. As it can be seen, no significant differences exist between the average slopes neither for O/H nor for N/O as a function of the presence of a bar in this sample of galaxies, although there is a slight trend to find flatter O/H gradients in barred galaxies. The difference in the N/O slopes of barred and unbarred galaxies is even smaller. This slight difference within the errors is still obtained when galaxies with an inclinations > 70^o are ruled out, as the detection of a bar is more difficult in these objects.

The possible abundance gradient flattening as a function of the presence of a bar is not observed by Sánchez et al. (2014); Marino et al. (2016) using partially the same data but a different methodology for the calculation of O/H. A similar result is obtained by Sánchez-Blázquez et al. (2014) for a subsample of face-on spiral galaxies, where no difference is found for the gradients of stellar age and Z as a function of the presence of a bar.

Regarding the characteristic chemical abundance ratios at the effective radius, there are not apparent large differences between the O/H values found for barred and unbarred galaxies, but a slight trend to find higher N/O values for barred galaxies is found. This difference is not statistically significant, but it cannot be owing to any bias in the stellar masses of the three subsamples defined as a function of the presence of a bar. The mean stellar mass for the three subgroups are log(M/M$_\odot$) = 10.01 for A galaxies, 10.08 for AB, and 10.23 for B, what would represent an enhancement of 0.01 dex for O/H and 0.04 dex for N/O according to the results described in above subsections. On the other hand these results agree with the differences of chemical abundances in the centres of barred galaxies found by Florido et al. (2015) which point to an enhancement of N/O in barred galaxies, while they do not find any difference when the studied ratio is O/H. This difference in N/O and not in O/H in the centres of barred galaxies could be due to a different star formation efficiency in the inner parts of galaxies as a consequence of the influence of bar-driven flows of gas.

7. An insight on flat and inverted gradients

A non negligible fraction of the 201 non-interacting galaxies in the CALIFA survey studied in this paper shows flat or positive gradients of O/H and/or N/O. Depending on the obtained associated errors of the slopes, the fraction of galaxies with an inverted slope varies from 10% up to 19% in the case of O/H and from 4.5% up to 10% in the case of N/O. There is not a complete coincidence between the galaxies that present inverted gradients of O/H and N/O (i.e. only 7 out of the 20 galaxies with an inverted N/O gradient have also an inverted O/H gradient).

As shown in previous sections, there is a slight, though not statistically significant, trend to find flatter gradients in less luminous and massive galaxies and in the earliest morphological types. However, there is not any clear difference between the average integrated properties of the galaxies with an inverted gradient as compared with the whole sample. The average absolute g luminosity and stellar mass for the 201 galaxies are -20.41 mag and $10^{10.09}$ M$_\odot$, respectively, while these numbers are only marginally different for galaxies with an inverted O/H (-20.13 mag and $10^{9.97}$ M$_\odot$) or N/O gradient (-20.36 mag and $10^{10.07}$ M$_\odot$).

For the rest of the integrated properties the observed relations with abundance slopes look to be caused by the relation with the stellar mass. Therefore there are neither much differ-

Table 3. Average slopes and values at the effective radius for the linear fittings of O/H and N/O in the analysed CALIFA galaxies for categories attending the observed morphology and the presence of a bar.

Type	Number	%	$\alpha_{O/H}$ (dex/R$_e$)	12+log(O/H) (at R$_e$)	$\alpha_{N/O}$ (dex/R$_e$)	log(N/O) (at R$_e$)
Morphology						
Sa-ab	17	8.5	-0.022 ± 0.081	8.721 ± 0.076	-0.113 ± 0.154	-0.926 ± 0.154
Sb	44	21.9	-0.046 ± 0.072	8.715 ± 0.052	-0.088 ± 0.088	-0.922 ± 0.125
Sbc	58	28.9	-0.085 ± 0.060	8.721 ± 0.052	-0.134 ± 0.091	-0.945 ± 0.124
Sc	37	18.4	-0.046 ± 0.068	8.678 ± 0.066	-0.088 ± 0.084	-1.091 ± 0.166
Scd	26	12.9	-0.048 ± 0.047	8.643 ± 0.044	-0.107 ± 0.084	-1.278 ± 0.120
Sd-I	19	9.4	-0.018 ± 0.062	8.590 ± 0.051	-0.065 ± 0.087	-1.359 ± 0.169
Presence of a bar						
A	89	44.3	-0.068 ± 0.067	8.680 ± 0.068	-0.102 ± 0.091	-1.071 ± 0.213
AB	53	26.4	-0.061 ± 0.075	8.678 ± 0.067	-0.109 ± 0.099	-1.061 ± 0.176
B	59	29.4	-0.041 ± 0.061	8.710 ± 0.073	-0.100 ± 0.101	-0.979 ± 0.182

ence in these other properties between the whole sample and the subset of galaxies with an inverted O/H or N/O gradient. The average colours, morphological type, and classes as a function of the presence of a bar are almost identical for galaxies with inverted and negative gradients.

It has been proposed that the flows of gas throughout and across the galaxy discs can sensibly alter the observed radial distribution of the metals (e.g. Kewley et al. 2010). In the case of our sample, interacting objects were ruled out, but should not be discarded the effect of minor mergers or past interactions in a recent period, after which the usual gradient shape has not been yet recovered (e.g. Miralles-Caballero et al. 2014). Positive abundance gradients have been also observed in low-massive gas-rich galaxies where a radial gas redistribution has possibly taken place (e.g. NGC 2915, Werk et al. 2010).

In this sense, a flat or inverted gradient can be the evidence of an absence of correlation of the radial abundance distribution more than the existence of an homogeneous Z throughout the disc. For our sample the mean correlation coefficient of the calculated linear fittings for galaxies with a negative gradient is -0.29 for O/H and -0.52 for N/O, while for inverted gradients is +0.20 for O/H and only +0.04 for N/O. This implies that positive gradients observed for N/O are mostly a consequence of a random abundance distribution throughout the discs. On the contrary, this is not so clearly observed in the case of O/H, once taken N/O into account for the derivation of O/H.

The simulations support the existence of positive gradients of Z after an interaction both in the local Universe (Rupke et al. 2010) and at larger z Tissera et al. (2016) and the drop of Z in the centres of galaxies after the fall of unprocessed gas (e.g. Lee et al. 2004). The fall of metal-poor gas from the exterior to explain the inverted gradients could be supported by the fact that the characteristic average O/H at the effective radius in these galaxies is lower. In Table 2 we see that O/H is 0.04 dex lower in average in these galaxies Besides, N/O characteristic value is almost identical with inverted O/H gradient, what partially would support the argument of the infall of metal-poor gas, as N/O tio is not expected to change substantially when a gas interchange is produced with the IGM medium (Edmunds 1990). On the contrary, galaxies with inverted N/O gradient present sensibly lower N/O characteristic values, what could be indicative or other causes for the inversion of the gradient, more related with the variation of the star formation efficient.

However, the influence of these gas flows should be also observed in the derived SFR and neither for the integrated SFR nor for sSFR any clear difference is seen between galaxies with an inverted gradient and the whole sample, as shown in subsection 6.2. At same time, we do not observed that the mean Hα luminosity of the H II regions in galaxies with an inverted gradient is higher (L(Hα = $10^{39.03}$ erg/s for regions in galaxies with positive O/H slope and $10^{39.13}$ erg/s for all H II regions) as seen in Fig. 15. The mean O/H and N/O are also the same in both sets of H II regions.

An inner gas transportation and redistribution from the galaxies centres towards the outer positions could be also supported by the observation of the flattening of the Z gradient beyond 2·R$_e$ (e.g. Bresolin et al. 2009; Rosales-Ortega et al. 2011; Marino et al. 2012; Sánchez et al. 2014). Additionally, it has been observed a decrease of Z in the inner regions of spiral galaxies in the radial range 0.3-0.5 R$_e$ (e.g. Rosales-Ortega et al. 2011; Sánchez et al. 2012b, 2014) possibly related to an accumulation of gas in rings, that can make flatter the resulting slopes of the Z gradients. For this work, no restriction was made in the fitted radial range Nevertheless, these two factors can have a certain influence in the fraction of observed flat or inverted gradients in our sample. By restricting the analysed H II regions to the range 0.5 - 2.1 · R$_e$, the number of galaxies with at least 10 H II regions is reduced to 147. For these the average slopes are -0.065 dex/R$_e$ for O/H and -0.115 dex/R$_e$ for N/O, which are slightly more pronounced than for the whole galaxy. The respective fractions of objects with an inverted gradient oscillates depending on the error from 9% up to 17% in the case of O/H and from 2% up to 12% for N/O.

Another factor that can have an influence on the calculations and thus can bias the results towards flatter abundance gradients is the inclination of the galaxies. Sánchez et al. (2014) only use objects with an inclination lower than 70^o in order to sample H II regions at all galactocentric distances and to avoid a bias towards the regions at outer distances. We calculated the inclinations using the ratio of the semi axis (b/a) measured over the photometric growth curves given by Walcher et al. (2014) and we used the same restriction than Sánchez et al. (2014), what reduces the sample of analysed galaxies to 113. The average slopes for these are -0.063 dex/R$_e$ for O/H and -0.125 dex/R$_e$ for N/O. The respective fractions of objects with an inverted gradient in this subsample ranges from 6% up to 15% for O/H and from 1% up to 4% for N/O. By combining this sub-sample of objects with an inclination lower than 70^o with the fitting in the radial range 0.5-2.1 R$_e$ (98 galaxies) the average slope is of -0.062 dex/R$_e$ for O/H and -0.113 dex/R$_e$ for N/O. The fraction of galaxies with an inverted gradients ranges from 11% up to 19% for O/H and from 1% up to 8% for N/O. For this same subsample, by making calculations assuming the O/H values derived by HCm without a previous determination of N/O and assuming a typical O/H-N/O relation, we obtained an average O/H slope of -0.095 dex/R$_e$ and a very high p-value in the Lilliefors normality test (0.94), what approximates very accurately the results obtained by Sánchez et al. (2014).

8. Summary and conclusions

In this work we studied the O/H and N/O abundance ratios of the ionised gas-phase in individual H ii regions and the radial distributions of these abundances across the discs in a sample of 351 galaxies using the spatially resolved IFS data from the CALIFA survey Sánchez et al. (2012a).

The abundances were derived in the selected star-forming H ii regions using the semi-empirical code HCm (Pérez-Montero 2014), based on photoionisation models. This code allows the derivation of O/H, N/O and log U covering a wide range of input values and **it is totally consistent with the direct method when the resulting abundances are compared in samples of objects with measured electron temperature, as in Pérez-Montero (2014).** This method takes the dependence of [N ii] emission lines on nitrogen abundances into account before its use to derive Z. The analysis of the O/H-N/O relation for the selected star-forming regions reveals a large dispersion and the resulting abundances can lie in regions of the diagram beyond the typical production of secondary N for a given Z. The range of variation of N/O in this sample [-1.8,-0,5] is much larger than for O/H [8.4,8.9] with a similar associated error, what supports that N/O can be a much more accurate indicator of the chemical status of an object than O/H.

The analysis of the radial distributions both for O/H and N/O normalised to the effective radius in those non-interacting galaxies with at least 10 star-forming H ii regions (201 galaxies) shows that most of the galaxies present a negative gradient although with large dispersion, with a mean slope α = -0.053 ± 0.068 dex/R$_e$ for O/H and α = -0.104 ± 0.096 dex/R$_e$ for N/O. In fact, a non-negligible fraction of galaxies present flat or even inverted gradients (at least a 10% for O/H and 4% for N/O). A correlation between O/H and N/O slopes exists (ρ_s = 0.39) but with large dispersion and even different combinations of O/H and N/O gradients can co-exist. This fact reveals the importance of a previous determination of N/O when [N ii] lines are used to derive O/H.

Contrary to individual H ii regions, for which the relation between O/H and N/O shows a very large dispersion and a relatively low correlation (ρ_s = 0.37), the characteristic O/H and N/O values (i.e. the values of the linear fittings at the effective radius) are well correlated (ρ_s = 0.80) and with a very low dispersion (i.e. the standard deviation of the residuals is of 0.12 dex) what supports the idea that the global chemical conditions of a galaxy is mostly related with their integrated properties regardless of its inner spatial variations. This has been also observed for the CALIFA sample of galaxies for the stellar population properties (González Delgado et al. 2015).

When analysing the distribution of slopes as a function of the galactic integrated properties, we see that galaxies with low stellar masses and absolute g luminosities tend to have flatter gradients, once normalised by the effective radius, both for O/H and N/O, but this result is not statistically significant. The same occurs with the morphological type, as early and late spiral galaxies have flatter gradients than intermediate type objects. In addition, no significant variation of the median slopes is found as a function of the presence of a bar. These results agree with the analysis made for other samples of these CALIFA galaxies using other strong-line methods for H ii regions (Sánchez et al. 2014; Marino et al. 2016), in the analysis spaxel-to-spaxel (Sánchez-Menguiano et al. 2016) or even from the analysis of the stellar abundances (Sánchez-Blázquez et al. 2014).

Regarding the characteristic O/H and N/O values at the effective radius, both the MZR and the MNOR are recovered with very low dispersion (i.e. the standard deviation of the residuals to a quadrant fitting is around 0.03 dex for both abundance ratios), confirming that these global relations are better obtained when the characteristic value of a galaxy, independently of the inner spatial variations, is used. We also observe clear relations between these characteristic abundances for each galaxy and other integrated properties, but all of them can be interpreted on the light of the MZR or the MNOR. In this way, although clear relation are observed between both O/H or N/O with the integrated present-day SFR and sSFR, these are owing to the M-SFR relation followed by all these objects. The observed M-SFR-Z-N/O relation makes even to observe a certain correlation between L(Hα) and O/H (or N/O) for the individual H ii regions of the galaxies in this sample. This absence of an additional dependence between O/H with SFR, as well as with N/O in the regime of secondary production of nitrogen, agrees with the results found by Sánchez et al. (2013) for the sample of H ii regions in CALIFA galaxies. We also observe clear correlations between abundances with integrated colours and morphology but, again, these are understood in terms of a sequence of earlier types and redder colours for more massive galaxies in this sample as also seen by (González Delgado et al. 2015).

Finally, we explored the nature of those objects with flat and inverted gradients of Z and N/O, but we did not find any special feature in these objects that can explain the inversion of the chemical gradient in the whole radial range. No significant variations in the average slopes or the fraction of inverted gradients are found when additional restrictions are taken related with the fitted radial range or the inclination of the galaxies, although these make the proportion of these gradients to be more reduced. A deeper inspections of these galaxies considering the past history of minor interactions, gas accretion and radial flows should be considered in order to understand that causes of these flat radial abundance distributions.

Acknowledgements. This study makes uses of the data provided by the Calar Alto Legacy Integral Field Area (CALIFA) survey (http://califa.caha.es/). CALIFA is the first legacy survey being performed at Calar Alto. The CALIFA collaboration would like to thank the IAA-CSIC and MPIA-MPG as major partners at the observatory, and CAHA itself, for the unique access to telescope time and support in manpower and infrastructures. The CALIFA collaboration also thanks the CAHA staff for their dedication to this project. EPM, JMV, CK, SP, and JIP acknowledge support from the Spanish MICINN through grants AYA2010-21887-C04-01 and AYA2013-47742-C4-1-P and the Junta de Andalucía for grant EXC/2011 FQM-7058. RGB, RGD, and EP acknowledge support from grants AYA2014-57490-P and JA-FQM-2828. Support for LG is provided by the Ministry of Economy, Development, and Tourism's Millennium Science Initiative through grant IC120009, awarded to The Millennium Institute of Astrophysics, MAS. LG acknowledges support by CONICYT through FONDECYT grant 3140566. This research made use of python (http://www.python.org), of Matplotlib (Hunter 2007), a suite of open-source python modules that provides a framework for creating scientific plots. We also thank Dr. Christophe Morisset for many discussions and constructive comments that have helped to improve the original manuscript.

References

Alloin, D., Collin-Souffrin, S., Joly, M., & Vigroux, L. 1979, A&A, 78, 200

Amorín, R. O., Pérez-Montero, E., & Vílchez, J. M. 2010, ApJ, 715, L128
Baldwin, J. A., Phillips, M. M., & Terlevich, R. 1981, PASP, 93, 5
Barrera-Ballesteros, J. K., Sánchez, S. F., García-Lorenzo, B., et al. 2015, A&A, 579, A45
Bresolin, F., Kennicutt, R. C., & Ryan-Weber, E. 2012, ApJ, 750, 122
Bresolin, F., Ryan-Weber, E., Kennicutt, R. C., & Goddard, Q. 2009, ApJ, 695, 580
Brinchmann, J., Charlot, S., White, S. D. M., et al. 2004, MNRAS, 351, 1151
Bryant, J. J., Owers, M. S., Robotham, A. S. G., et al. 2015, MNRAS, 447, 2857
Bundy, K., Bershady, M. A., Law, D. R., et al. 2015, ApJ, 798, 7
Cardelli, J. A., Clayton, G. C., & Mathis, J. S. 1989, ApJ, 345, 245
Carton, D., Brinchmann, J., Wang, J., et al. 2015, MNRAS, 451, 210
Cid Fernandes, R., Pérez, E., García Benito, R., et al. 2013, A&A, 557, A86
Cid Fernandes, R., Stasińska, G., Mateus, A., & Vale Asari, N. 2011, MNRAS, 413, 1687
Contini, T., Garilli, B., Le Fèvre, O., et al. 2012, A&A, 539, A91
Cresci, G., Mannucci, F., Maiolino, R., et al. 2010, Nature, 467, 811
Diaz, A. I. 1989, in Evolutionary Phenomena in Galaxies, ed. J. E. Beckman & B. E. J. Pagel, 377–397
Dopita, M. A. & Evans, I. N. 1986, ApJ, 307, 431
Edmunds, M. G. 1990, MNRAS, 246, 678
Ellison, S. L., Patton, D. R., Simard, L., & McConnachie, A. W. 2008, ApJ, 672, L107
Evans, I. N. & Dopita, M. A. 1985, ApJS, 58, 125
Falcón-Barroso, J., Sánchez-Blázquez, P., Vazdekis, A., et al. 2011, A&A, 532, A95
Ferland, G. J., Porter, R. L., van Hoof, P. A. M., et al. 2013, Rev. Mexicana Astron. Astrofis., 49, 137
Florido, E., Zurita, A., Pérez, I., et al. 2015, A&A, 584, A88
García-Benito, R., Zibetti, S., Sánchez, S. F., et al. 2015, A&A, 576, A135
Garnett, D. R. & Shields, G. A. 1987, ApJ, 317, 82
Garnett, D. R., Shields, G. A., Skillman, E. D., Sagan, S. P., & Dufour, R. J. 1997, ApJ, 489, 63
González Delgado, R. M., García-Benito, R., Pérez, E., et al. 2015, A&A, 581, A103
Ho, I.-T., Kudritzki, R.-P., Kewley, L. J., et al. 2015, MNRAS, 448, 2030
Hunter, J. D. 2007, Computing In Science & Engineering, 9, 90
Kauffmann, G., Heckman, T. M., Tremonti, C., et al. 2003, MNRAS, 346, 1055
Kehrig, C., Monreal-Ibero, A., Papaderos, P., et al. 2012, A&A, 540, A11
Kelz, A., Verheijen, M. A. W., Roth, M. M., et al. 2006, PASP, 118, 129
Kewley, L. J., Dopita, M. A., Sutherland, R. S., Heisler, C. A., & Trevena, J. 2001, ApJ, 556, 121
Kewley, L. J., Groves, B., Kauffmann, G., & Heckman, T. 2006, MNRAS, 372, 961
Kewley, L. J., Rupke, D., Zahid, H. J., Geller, M. J., & Barton, E. J. 2010, ApJ, 721, L48
Köppen, J. & Hensler, G. 2005, A&A, 434, 531
Lamareille, F., Mouhcine, M., Contini, T., Lewis, I., & Maddox, S. 2004, MNRAS, 350, 396
Lara-López, M. A., Cepa, J., Bongiovanni, A., et al. 2010, A&A, 521, L53
Lee, J. C., Salzer, J. J., & Melbourne, J. 2004, ApJ, 616, 752
Lequeux, J., Peimbert, M., Rayo, J. F., Serrano, A., & Torres-Peimbert, S. 1979, A&A, 80, 155
Lilly, S. J., Le Fèvre, O., Renzini, A., et al. 2007, ApJS, 172, 70
López-Sánchez, Á. R. & Esteban, C. 2010, A&A, 517, A85
López-Sánchez, Á. R., Westmeier, T., Esteban, C., & Koribalski, B. S. 2015, MNRAS, 450, 3381
Mannucci, F., Cresci, G., Maiolino, R., Marconi, A., & Gnerucci, A. 2010, MNRAS, 408, 2115
Marino, R. A., Gil de Paz, A., Castillo-Morales, A., et al. 2012, ApJ, 754, 61
Marino, R. A., Gil de Paz, A., Sánchez, S. F., et al. 2016, A&A, 585, A47
Marino, R. A., Rosales-Ortega, F. F., Sánchez, S. F., et al. 2013, A&A, 559, A114
Mattsson, L. 2009, in IAU Symposium, Vol. 254, IAU Symposium, ed. J. Andersen, Nordströara, B. m, & J. Bland-Hawthorn, 43P
Miralles-Caballero, D., Díaz, A. I., Rosales-Ortega, F. F., Pérez-Montero, E., & Sánchez, S. F. 2014, MNRAS, 440, 2265
Mollá, M., García-Vargas, M. L., & Bressan, A. 2009, MNRAS, 398, 451
Mollá, M., Vílchez, J. M., Gavilán, M., & Díaz, A. I. 2006, MNRAS, 372, 1069
Moran, S. M., Heckman, T. M., Kauffmann, G., et al. 2012, ApJ, 745, 66
Moustakas, J. & Kennicutt, Jr., R. C. 2006, ApJS, 164, 81
Pérez-Montero, E. 2014, MNRAS, 441, 2663
Pérez-Montero, E. & Contini, T. 2009, MNRAS, 398, 949
Pérez-Montero, E., Contini, T., Lamareille, F., et al. 2013, A&A, 549, A25
Pérez-Montero, E. & Díaz, A. I. 2005, MNRAS, 361, 1063
Pérez-Montero, E. & Vílchez, J. M. 2009, MNRAS, 400, 1721
Pérez-Montero, E., Vílchez, J. M., Cedrés, B., et al. 2011, A&A, 532, A141
Pichon, C., Pogosyan, D., Kimm, T., et al. 2011, MNRAS, 418, 2493
Pilyugin, L. S. & Grebel, E. K. 2016, MNRAS, 457, 3678
Pilyugin, L. S., Vílchez, J. M., & Contini, T. 2004, A&A, 425, 849
Queyrel, J., Contini, T., Kissler-Patig, M., et al. 2012, A&A, 539, A93
Rich, J. A., Torrey, P., Kewley, L. J., Dopita, M. A., & Rupke, D. S. N. 2012, ApJ, 753, 5
Roberts, M. S. & Haynes, M. P. 1994, ARA&A, 32, 115
Rosales-Ortega, F. F., Díaz, A. I., Kennicutt, R. C., & Sánchez, S. F. 2011, MNRAS, 415, 2439
Rosales-Ortega, F. F., Sánchez, S. F., Iglesias-Páramo, J., et al. 2012, ApJ, 756, L31
Roth, M. M., Kelz, A., Fechner, T., et al. 2005, PASP, 117, 620
Rupke, D. S. N., Kewley, L. J., & Chien, L.-H. 2010, ApJ, 723, 1255
Sánchez, S. F., García-Lorenzo, B., Jahnke, K., et al. 2006, New A Rev., 49, 501
Sánchez, S. F., Kennicutt, R. C., Gil de Paz, A., et al. 2012a, A&A, 538, A8
Sánchez, S. F., Rosales-Ortega, F. F., Iglesias-Páramo, J., et al. 2014, A&A, 563, A49
Sánchez, S. F., Rosales-Ortega, F. F., Jungwiert, B., et al. 2013, A&A, 554, A58
Sánchez, S. F., Rosales-Ortega, F. F., Kennicutt, R. C., et al. 2011, MNRAS, 410, 313
Sánchez, S. F., Rosales-Ortega, F. F., Marino, R. A., et al. 2012b, A&A, 546, A2
Sánchez-Blázquez, P., Rosales-Ortega, F. F., Méndez-Abreu, J., et al. 2014, A&A, 570, A6
Sánchez-Menguiano, L., Sánchez, S. F., Pérez, I., et al. 2016, ArXiv e-prints
Skillman, E. D. 1989, ApJ, 347, 883
Storey, P. J. & Hummer, D. G. 1995, MNRAS, 272, 41
Thuan, T. X., Pilyugin, L. S., & Zinchenko, I. A. 2010, ApJ, 712, 1029
Tissera, P. B., Pedrosa, S. E., Sillero, E., & Vilchez, J. M. 2016, MNRAS, 456, 2982
Tremonti, C. A., Heckman, T. M., Kauffmann, G., et al. 2004, ApJ, 613, 898
Troncoso, P., Maiolino, R., Sommariva, V., et al. 2014, A&A, 563, A58
van Zee, L. & Haynes, M. P. 2006, ApJ, 636, 214
Vazdekis, A., Sánchez-Blázquez, P., Falcón-Barroso, J., et al. 2010, MNRAS, 404, 1639
Veilleux, S. & Osterbrock, D. E. 1987, ApJS, 63, 295
Vila-Costas, M. B. & Edmunds, M. G. 1992, MNRAS, 259, 121
Walcher, C. J., Wisotzki, L., Bekeraité, S., et al. 2014, A&A, 569, A1
Werk, J. K., Putman, M. E., Meurer, G. R., & Santiago-Figueroa, N. 2011, ApJ, 735, 71
Werk, J. K., Putman, M. E., Meurer, G. R., et al. 2010, ApJ, 715, 656
Zaritsky, D., Kennicutt, Jr., R. C., & Huchra, J. P. 1994, ApJ, 420, 87